Accepted Manuscript

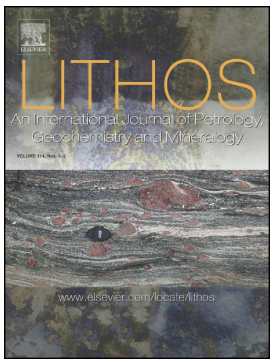

Constraining deformation phases in the Aar Massif and the Gotthard Nappe (Switzerland) using Th-Pb crystallization ages of fissure monazite-(Ce)

E. Ricchi, C.A. Bergemann, E. Gnos, A. Berger, D. Rubatto, M.J. Whitehouse

PII: S0024-4937(19)30163-X
DOI: https://doi.org/10.1016/j.lithos.2019.04.014
Reference: LITHOS 5043

To appear in: *LITHOS*

Received date: 20 November 2018
Accepted date: 19 April 2019

Please cite this article as: E. Ricchi, C.A. Bergemann, E. Gnos, et al., Constraining deformation phases in the Aar Massif and the Gotthard Nappe (Switzerland) using Th-Pb crystallization ages of fissure monazite-(Ce), LITHOS, https://doi.org/10.1016/j.lithos.2019.04.014

Constraining deformation phases in the Aar Massif and the Gotthard Nappe (Switzerland) using Th-Pb crystallization ages of fissure monazite-(Ce)

E. Ricchi[1], C.A. Bergemann[1, 2], E. Gnos[2], A. Berger[3], D. Rubatto[3, 4], M.J. Whitehouse[5]

[1]*Department of Earth Sciences, University of Geneva, Rue des Maraîchers 13, 1205 Geneva, Switzerland*

[2]*Natural History Museum of Geneva, Route de Malagnou 1, 1208 Geneva, Switzerland*

3 Institut de Sciences de la Terre, University of Lausanne, Geopolis, 1015 Lausanne, Switzerland

[4] *Institute of Geological Sciences, University of Bern, Baltzerstrasse 1+3, 3012 Bern, Switzerland*

[5]*Swedish Museum of Natural History, Stockholm, Sweden*

Abstract

Fissure monazite-(Ce) (hereafter called monazite) commonly crystallises during deformation at low metamorphic grade and offers the possibility to date protracted deformation over several millions of years and to identify distinct deformation phases. We performed Th-Pb geochronology at the microscale on 10 samples of fissure monazite from two Alpine crystalline massifs (Aar Massif and Gotthard Nappe). Ion microprobe ages show that the earliest stage of crystallization recorded by fissure monazite domain ages occurred around 15.9 Ma in the Gotthard Nappe and about 1 My later in the Aar Massif, with the latest crystallization event recorded at 6 Ma. Protracted monazite crystallization in fissures indicates that deformation datable with fissure monazite lasted about 10 Ma.

Comparison of Th-Pb crystallization ages of fissure monazite to existing thermochronological data shows that early monazite crystallization coincide with zircon fission track ages, whereas the youngest monazite crystallization overlaps with apatite fission track ages. Monazite also grows contemporaneous with muscovite/illite crystallization (K-Ar ages) in fault gouges. As

monazite can grow during dissolution/precipitation cycles induced by tectonic activity, their chronology allows to further constrain in the Aar Massif the final Handegg phase at 12 – 11.5 Ma, and the coeval activity of the Pfaffenchopf (11.5 – 9 Ma), and the Oberaar and Rhone-Simplon phases (11.5 and 6 Ma). In the Gotthard Nappe, monazite crystallization constrains a major portion of the Chièra backfolding phase at 14-13 Ma, and confirms that the south-western termination of the nappe was affected by the Rhone-Simplon phase.

Keywords

Hydrothermal monazite-(Ce); Alpine fissures; Th-Pb dating; Tectonic phases; Aar Massif; Gotthard Nappe

1. Introduction

The temporal evolution of deformation, uplift and cooling in orogens has been mainly investigated through thermochronology, as for example fission track dating (e.g. Berger et al., 2017; Glotzbach et al., 2010; Michalski and Soom, 1990; Pleuger et al., 2012; Reinecker et al., 2008). This approach has however the disadvantage that direct relations of ages to structures are often missing. A better link with structures can possibly be established by using minerals that form in specific deformation features such as micas and illites (e.g., Campani et al., 2010; Kralik et al., 1992; Rolland et al, 2008; Wiederkehr et al., 2009) or monazites in clefts (Bergemann et al., 2017; Berger et al., 2013; Gasquet et al., 2010; Gnos et al., 2015; Grand'Homme et al., 2016a; Janots et al., 2012). The advantage of being diffusion-independent in the fissure monazite approach (the Th-U-Pb system being not affected by diffusion under fissure monazite conditions; e.g. Cherniak et al., 2004) is partly counterbalanced by the complex fluid dynamics in fissures and the potentially complex mineral growth (e.g. Grand'Homme et al., 2016b; Seydoux-Guillaume et al., 2012).

Studies on a few fissure monazites form the Aar Massif and the Gotthard Nappe (Bergemann et al., 2017; Berger et al., 2013; Janots et al., 2012) yielded growth domain ages ranging from 15.5 ± 0.2 to 6.25 ± 0.60 to Ma (Fig. 1). In some of these studies it has been shown that the monazite domains date fault activity in a temperature window of ~350 - 200°C (lower greenschist to sub-greenschist facies conditions) in which fissure monazite crystallizes. The goal of this study is to provide monazite crystallization ages for all regions of the two massifs in order to better constrain some of the known deformation phases compiled in Table 1.

Fissures occur in various rock types, and generally form at temperatures below ~500 °C, i.e. near or below the ductile to brittle transition (e.g., Mullis, 1996; Stalder et al., 1998). Fissure formation probably occurs under fluid-assisted cracking of the rock (e.g., Cox, 2010). They are generally oriented perpendicular to the foliation and lineation of the rock (Bergemann et al., 2017; Berger et al., 2013; Gnos et al., 2015; Janots et al., 2012). Independent of fissure orientation, the age record of monazite starts only when monazite crystallization conditions are reached (~350-200 °C, Bergemann et al., 2017; Gnos et al., 2015). This can occur late in a cleft history, under the same or a different stress field (e.g. Bergemann et al., 2019).Whenever the fissure fluid comes into chemical disequilibrium, leaching of the surrounding host rock leads to the precipitation of hydrothermal minerals in the fissure (e.g., Mercolli et al., 1984), until equilibrium is reestablished. The fluid-filled fissures containing monazite represent a system sensitive to deformation (e.g. Bergemann et al., 2017, 2018; Janots et al., 2012). Each deformation (e.g. by change of shape, exposure of fresh host rock, propagation of the fissure) causes chemical disequilibrium between fluid, fissure minerals and host rock. Such changing conditions in turn lead to a dissolution/precipitation cycle and partial recrystallization of monazite and resetting of its U-Th-Pb system. Due to this fluid-enhanced reactivity, monazite dissolution/precipitation reactions can easily take place in fluid-filled fissures, whereas this is rarely observable in the surrounding rocks. Thus geochronology of fissure monazite permits

to indirectly date brittle deformation (Bergemann et al., 2017; Berger et al., 2013) at temperatures below ~300°C (e.g. Gnos et al., 2015), a temperature range usually only accessible by fault gauge dating (e.g., Kralik et al., 1992; Pleuger et al., 2012).

Therefore, Th-U-Pb dating of fissure monazite grains has to be combined with careful textural and petrographic investigation. The relatively large grain size of fissure monazite (up to ~2 mm) can allow the determination of different growth ages in texturally and chemically distinct domains. Such monazite growth zones are mainly due to fluid dynamics in fissures, changes in which are controlled by the stress field and related deformation, and by chemical disequilibrium. The initiation of the fissure formation (and their orientation) is directly related to the deformation phase, whereas change in the orientation of a deformation in combination with low strain may only lead to changes in fluid dynamics, but not necessary in a complete reorientation of the fissure (e.g. Bergemann et al., 2017). We applied this method to fissure monazite from the AM and from the GN. Preference was given to monazite grains collected near fault zones in order to constrain fault activity and to correlate deformation stages with monazite Th-Pb crystallization ages from horizontal and vertical fissures. In order to do so, we present detailed isotopic data and connect them with the known deformation phases in the area. This approach allows detailed constraints of the evolution steps in the brittle field during cooling of the area. The results are tested against available thermochronological data (zircon/apatite fission tracks, Th(U-He)-ages; Glotzbach et al., 2010; Michalski and Soom, 1990; Reinecker et al., 2008; Valla et al., 2012; Vernon et al., 2009; Wagner, 1977).

The monazite lattice ((LREE,Th)PO_4) has a high resistance to radiation damage (e.g., Meldrum et al., 1998), and in the low-temperature environment where hydrothermal monazite crystallizes (<400°C; Grand'Homme et al., 2016b) Pb diffusion is negligible (e.g., Cherniak et al., 2004). The isotopic systems in monazite can only be reset by recrystallization or

dissolution/reprecipitation, notably in the presence of hydrous fluids (e.g., Cherniak et al., 2004; Cherniak and Pyle, 2008; Grand'Homme et al., 2016b; Seydoux-Guillaume et al., 2012, 2002). Due to the presence of hydrous fluids in fissures, retrograde mineral reactions are common. Thorium-U-Pb dating of hydrothermal monazite is therefore a robust geochronological method that provides information on the crystallization ages and crystallization duration of hydrothermal monazite within a fissure, reflecting fissure chemical variations due to multiple circulation of fluids, repeated tectonic activity (Bergemann et al., 2017; Berger et al., 2013; Gnos et al., 2015; Grand'Homme et al., 2016a; Janots et al., 2012) or other factors leading to chemical disequilibrium. In the ideal case total dissolution and precipitation of a new monazite would erase the Th-U-Pb isotopic compositions of the parent monazite. Given that the monazite lattice does not incorporate Pb during crystallization, all the Pb present in monazite should be radiogenic, providing new and undisturbed Th-U-Pb ages. However, experimental work showed that the dissolution/re-precipitation process can influence the Th-U-Pb geochronometer and care has to be taken when interpreting monazite ages. When dating a primary monazite, age underestimation (Pb loss) is possible due to the anisotropic dissolution and replacement of monazite at the nanoscale. For the same reason, excess lead resulting from the presence of nano-remnants of primary monazite in a secondary monazite can induce age overestimation (Grand'Homme et al., 2018, 2016b). During dissolution/re-precipitation, monazite is also likely to incorporate Pb as clusters or Pb-rich inclusions at the nanoscale (Pb excess) resulting in particularly old ages (Seydoux-Guillaume et al., 2018, 2003).

2. Geologic background

The collision of the European and the Adriatic continental plates initiated in the Mesozoic and led to several phases of deformation that can be studied today in exposures within the Alps

(e.g., Ford et al., 2006; Schmid et al., 2004). The AM and the GN, located in the Swiss Central Alps (Fig. 1), are composed of a polymetamorphic basement, Variscan volcanic and plutonic rocks and Mesozoic sedimentary rocks (e.g. Berger et al., 2017). The Alpine metamorphic grade increases from sub-greenschist facies in the north of the AM to upper greenschist facies in the south of the GN (Bousquet et al., 2012).

In the late Oligocene the transition from subduction to continent-continent collision occurred. Compression, together with mantle rollback, continued until the middle Miocene and allowed the progressive delamination of the European lithosphere, resulting in the emplacement of the GN onto the southern AM (e.g. Herwegh et al., 2017, Fig. 2a; D2 phase in Table 1). The Helvetic sedimentary cover was detached and transported towards the North (Calanda and Kiental deformation phases in Table 1) and later, buoyancy forces promoted the vertical uplift of the AM (e.g. Berger et al., 2017; Herwegh et al., 2017). This crustal thickening triggered the development of steep reverse faults inside the AM, known as the Handegg phase and induced the folding of the GN, known as Chièra and Berisal phase in the East and West of the GN, respectively (e.g. Berger et al., 2017; Mair et al., 2018; Wehrens et al., 2017; Table 1 and Fig. 2b). Subhorizontal fissures were formed during these two deformation phases. During the middle to late Miocene the European slab rollback ceased, progressively resulting in transpressional conditions at the southern border of the AM, leading to dextral strike-slip in this area known as the Oberaar deformation phase (Fig. 2c) which lasted from 11.5 to at least 7 Ma (Bergemann et al., 2017; Rolland et al., 2008; Rossi and Rolland, 2014; Wehrens et al., 2017, Table1). Contemporaneously, NW-directed horizontal thrust affected the northern AM due to persisting compressional forces, known as the Pfaffenchopf phase (e.g. Berger et al., 2017; Herwegh et al., 2017; Mair et al., 2018; Wehrens et al., 2017). The Oberaar phases is related to subvertical fissure formation, but also to the reactivation and overprinting of horizontal fissures formed during the Handegg deformation (Fig. 2c). Strike-slip movements

also affected the southwestern limb of the AM forming subvertically-oriented fissures. In this area, Ar/Ar crystallization ages suggest that the deformation along the Rhone-Simplon fault occurred between 14.2–11 Ma (Campani et al., 2010; Rhone Simplon Phase in Table 1), and continued until at least 6.25 ± 0.60 Ma (Berger et al., 2013). This shows that the dextral Oberaar fault system was active at the same time as the parallel, dextral Rhone-Simplon fault.

In the specific region of this study it has been documented that horizontal fissures formed during steep reverse faulting in the AM (Handegg phase; Wehrens et al., 2017) and during the steepening of the GN linked to the emplacement of the Northern Steep Belt generation (Chièra phase; Berger et al., 2017; Herwegh et al., 2017; Milnes, 1976). The ensuing transpressive conditions within the AM (Oberaar phase of Wehrens et al., 2017 and Rhone-Simplon Line; Berger et al., 2017; Campani et al., 2010; Herwegh et al., 2017) led to the formation of vertical fissures and overprinting of the older horizontal fissure generation. In the Gotthard pass region of the GN, an overprinting of horizontal fissures by younger subvertical fissures similar to the AM has been observed (Heijboer, 2006).

3. Analytical techniques

Monazite identification was carried out using a mercury vapor lamp, an optical microscope and a Scanning Electron Microscope (SEM) at the Natural History Museum of Geneva and at the Department of Earth Sciences of the University of Geneva. The samples were embedded in epoxy and each sample was polished individually down to a central section of the monazite crystal. A total of up to seven monazite grains were then mounted together with standards in an epoxy disk before performing a final polishing step.

Backscatter electron (BSE) images of the mounted monazite grains were obtained using an EDS-quipped JEOL JSM7001F and a Zeiss DSM940A electron microscope at the University of Geneva using a beam current of 3.5 nA. BSE images mainly highlight zoning related to Th

variations (e.g. Bergemann et al., 2017), helping to select ion microprobe spot analysis points in the different growth domains of a grain. The surface of the mounts has to be flat for ion probe dating. For this reason, element mapping causing damage of the epoxy is not possible.

Thorium-U-Pb analyses of 7 samples (NEAT1, JOLI2, GAST1, MUTT1, UNTE1, CAVR1 and GOTT1) were performed at the SwissSIMS Ion microprobe facility, at the University of Lausanne, Switzerland (Tables 2 and 3), whereas 3 samples (GUTT1, GOSCH1 and SALZ21) were analysed at the Nordsim facility, Swedish Museum of Natural History in Stockholm (Tables 2 and 4). Both laboratory host a Cameca IMS 1280-HR instrument and the general instrumental set up follow the description of Janots et al., (2012). A -13 kV O_2- primary beam with an intensity of ca. 3 and 6 nA (SwissSIMS and Nordsim, respectively) was focused on the sample to produce a spot of 15-20 micron in diameter. Analyses were performed at a mass resolution of 4300–5000 (M/ΔM, at 10% peak height) and an energy window 40 eV, with data collected in peak hopping mode using an ion-counting electron multiplier.

Data were standardised to the 44069 monazite (425 Ma, Aleinikoff et al, 2006) and the uncertainty on the standard $^{208}Pb/^{232}$ Th – ThO/Th calibration were 1.00 to 1.81 % . A common lead (Pb_c) correction calculated at time zero (present-day) was applied using the terrestrial Pb evolution model of Stacey and Kramers (1975). In the text, uncertainties on single ages are quoted at 1 sigma level and weighted mean ages, hereafter called average ages, are quoted at 95% confidence level.

A ^{207}Pb-based correction was applied to the data NEAT1, JOLI2, GAST1, MUTT1, UNTE1, CAVR1 and GOTT1 (Table 3) and was preferred to ^{204}Pb-correction due to better counting statistics obtained on the ^{207}Pb isotope. Data treatment and standardisation was carried out using the SQUID software (Ludwig, 2009) and Isoplot 4.15 (Ludwig, 2003). No $^{232}Th^{143}Nd^{16}O_2^{++}$correction was needed for these samples due to the undetectable Nd peak. Data reduction for GUTT1, GOSCH1 and SALZ21 (Table 4) was done with the Cameca

Customisable Ion Probe Software (CIPS), including a very small ^{204}Pb-correction and $^{232}Th^{143}Nd^{16}O_2^{++}$ correction (see Bergemann et al., 2017). The program IsoPlot Ex 4.1 (Ludwig, 2003) was used for weighted average age calculations and plotting.

4. Samples and Results

4.1.Field observations

Fissure monazite is rare. For this reason, most of the selected hydrothermal monazite grains (Fig. 1), were collected by crystal searchers in fissures within the Aar Massif (NEAT1, JOLI2, GAST1, GUTT1, GOSCH1 and SALZ21) and the Gotthard Nappe (MUTT1, UNTE1, CAVR1 and GOTT1). Many of the localities are located in steep terrain and are not easily accessible, or do not exist anymore (for example tunnel outcrops). Thus the information compiled in Table 2 is largely based on information obtained from the crystal searchers.

Fissures and clefts form during tectonic movements under peak to retrograde metamorphic conditions and become filled with hydrothermal fluids. Fissures (Figs. 3a, b, c) are characterized by parallel wall surfaces whereas clefts walls tend to be curved (Fig. 3d). Clefts usually experienced several deformation cycles as confirmed by fluid inclusion studies (e.g., Mullis, 1996). However, only in rare cases (Fig. 3b) deformation stages are well visible in the field. The term fissure will be employed from now on for simplicity.

In the AM and GN, two orientations of monazite-bearing fissures are observed, horizontal and vertical (Table 1). Horizontal fissures are older (e.g. Bergemann et al., 2017). However, some fissures in the southern part of the GN dip to the south-east as folds developed during the formation of the Northern Steep Belt (NSB; Klaper, 1985; Milnes, 1974; Wiederkehr et al., 2008, 2009). Fissures are generally oriented perpendicular to the main foliation and lineation of the host-rock indicating the stress field conditions during initial fissure formation.

The fissures occur in varying host rocks (granite, gneiss, sericite gneiss, two-mica gneiss, sericite schist) that underwent Alpine metamorphism up to upper greenschist facies conditions (Table 2, Fig. 1; Bousquet et al., 2012).

4.2. Monazite chemistry and dating

The grains are mm sized and yellow to pinkish under natural light. A total of 185 individual Th-U-Pb measurements were performed (Table 3 and 4) with an average of 18 spots per grain in order to obtain geochronological and geochemical information.

In hydrothermal monazite, because of the high Th content and generally low U content the ^{232}Th-^{208}Pb ages are usually more robust and precise and the comparison of Th-Pb dates with U-Pb dates can be compromised (e.g., Janots et al. 2012). However, almost all the grains investigated in this study have ^{232}Th-^{208}Pb ages in agreement with ^{238}U-^{206}Pb ages (Table 3).

Monazite Th content mostly ranges from 1,600 to 95000 ppm, and is up to 210,000 ppm for CAVR1 grain. Some analyses have very high Th content but there is no clear correlation between Th and age so we suggest that there is not significant matrix effect. So these data have to be treated with caution. U content of the analysed monazites ranges from 12 to 2,400 ppm, resulting in high Th/U values of ~260 (up to 924 for NEAT1), typical for hydrothermal environments (Bergemann et al., 2017; Gnos et al., 2015; Grand'Homme et al., 2016a; Janots et al., 2012). This is also true for CAVR1 grain, displaying a Th/U ratio in the range 100-770. Electron microprobe analyses of SALZ21 and GOSCH1 (see data repository Table A.2 and Fig.R1) confirm that fissure monazite growing at temperature <350°C shows only small amount of Si, Ca and Y (<0.025 per formula unit), indicating very limited solid solution with huttonite ($ThSiO_4$), brabantite ($CaTh(PO_4)_2$) and xenotime (YPO_4).

Thorium versus U plots were produced for each monazite sample in order to identify chemical groups inside the mineral zones used for defining weighted average ages (Figs. 4 and 5).

Following the same strategy, age groups and/or ranges were determined for all the minerals combining chemical information and textural observations. Analyses resulting in unreliable dates (e.g. presence of cracks/dissolution spots, affected by Pb_c causing high uncertainty) were not considered and are written in italic in Tables 3 and 4.

4.3. Monazites from the Aar Massif

Monazite grain NEAT1 (Figs. 4a-c) consists of a main crystal, almost homogeneous in composition, and a recrystallized zone, with high porosity, formed by a multitude of crystallites (Fig. 4b). The rim of the main crystal (Fig. 4c, NEAT1-A) has a mean age of 12.22 ± 0.22 Ma (MSWD = 0.99, n = 5) and its chemistry is homogeneous compared to the other analysed samples (around 30,000 and 50 ppm of Th and U respectively, Fig. 4a). The inner part of the main crystal (NEAT1-B: 12.5 ± 1.2 Ma, MSWD = 4.2, n = 4) and a crystallite cluster (NEAT1-C: 12.1 ± 1.0 Ma, MSWD = 3.4, n = 4) show scattered dates which are close to the age provided by NEAT1-A rim. A larger scatter is observed for one of the crystallites (NEAT1-D) where the dates range from 11.79 ± 0.22 to 8.15 ± 0.15 Ma. Analyses 15 and 29 are affected by a crack and inclusion respectively (high resolution image, NEAT1_BSE.tif, available in data repository) and spots 11 to 14, showing high Pb_c with a high age uncertainty (Table 3), were not considered. The chemistry of the zones returning scattered dates (NEAT1-B, C and D) varies considerably but tends to follow a similar Th/U trend as the main crystal.

JOLI2 (Figs. 4d-f) is the youngest grain analysed in this study and displays two distinct chemical domains. Domain A represents the internal part of the grain with low Th (~3,700 ppm) and variable U (15-97 ppm) content whereas domain B corresponds to a lighter rim on BSE image related to higher Th (~11,000 ppm) and more clustered U content (~47 ppm; Figs. 4d and f). The calculated age for domain A (JOLI2-A: 8.3 ± 1.0 Ma, MSWD = 9.3, n = 6) and B (JOLI2-B: 8.24 ± 0.78 Ma, MSWD = 7.0, n = 4) is identical within error (Fig.

4f) and the higher age dispersion observed in the domain A is probably due to lower Th content. Spot 2 displays the youngest date but is affected by a thin crack (high resolution image, JOLI2_BSE.tif, available in data repository).

The geometry of GAST1 (Figs. 4g-i) suggests the growth of a monazite core (GAST1-A) with two chemically distinct rims (GAST1-B1 and B2, Fig. 4h). The core composition is quite homogeneous, ranging between 19-116 and 1,604-8,322 ppm of U and Th respectively, and giving a mean age of 11.15 ± 0.61 Ma (MSWD = 2.4, n = 12). GAST1-B1 rim is compositionally closer to the core composition (Th/U ratio ~174) compared to GAST1-B2 (Th/U ratio ~46), but both rims display similar ages of 9.99 ± 0.40 Ma (MSWD = 0.26, n = 3) and 9.4 ± 1.2 Ma (MSWD = 3.2, n = 3).

In GUTT1 monazite (Figs. 4j-l), domain A is related to higher Th content and corresponds to a lighter zone on BSE image compared to GUTT1-B (Fig. 4k). However, both domains provide dates ranging from 14 - 9 Ma. For this reason and due to the small number of analyses we only indicate a spot age range of 14.24 ± 0.94 Ma and 8.68 ± 0.62 Ma.

GOSCH1 monazite can be divided into three chemically distinct domains (GOSCH1-A, B and C; Figs. 4m and n), with an average Th/Pb ratio respectively decreasing from 189, 43 to 24 and corresponding to darker crystal zones observed on the BSE image. An average age of 11.99 ± 0.56 Ma (MSWD = 2.2, n = 7) is calculated for domain GOSCH1-B (Fig. 4o). Although chemically distinct, the two dates of domain GOSCH1-A overlap with the age of GOSCH1-B. GOSCH1-C displays an age range down to 8.94 ± 0.35 Ma. Spots 7 and 10 were not considered because they respectively sit on the grain edge and on a crack (Table 4).

In monazite SALZ21 (Figs. 4p-r), two domains are clearly identified according to the two distinct chemical trends visible on the Th-U plot (Fig. 4p). Domains SALZ21-A and B respectively display a Th/U ratio of ~156 and ~72 and very similar weighted mean ages of 10.90 ± 0.29 Ma (MSWD = 1.04, n = 5) and 10.63 ± 0.29 Ma (MSWD = 0.70, n = 5). Three

spots located near SALZ21-A zone yield younger dates ranging from 9.80 ± 0.30 Ma to 8.36 ± 0.29 Ma. These analyses are affected by dissolution trails depicted by red dashed lines on Fig. 4q (high resolution image, SALZ21_BSE.tif, available in data repository). and the corresponding dates may not be reliable due to Pb loss (Table 4).

4.4. Monazites from the Gotthard Nappe

Combining chemical, textural and geochronological information, MUTT1 monazite (Figs. 5a-c) can be divided into four main domains. MUTT1-A in the grain center yields the oldest age of 14.22 ± 0.97 Ma (MSWD = 1.8, n = 5) with Th and U contents ranging between 6,901-16,473 and 45-81 ppm. Domain MUTT1-B is similarly low in Th as MUTT1-A. MUTT1-C show patchy zoning and is more heterogeneous in composition (Th and U values ranging between 3,834-26,396 and 82-179 ppm respectively) and domain MUTT1-D has the lowest U content of ~18 ppm. The MUTT1-B, C and D domains ages at 13.10 ± 0.40 Ma (MSWD = 0.68, n = 4), 12.92 ± 0.48 Ma (MSWD = 1.2, n = 5) and 12.72 ± 0.35 Ma (MSWD = 1.2, n = 5) are overlapping. One analysis (spot 16) was not considered due to high Pb_c (Table 3).

UNTE1 monazite (Figs. 5d-f) displays oscillatory zoning and altered areas are visible in the core and the rim (patchy zones, Fig. 5e). Multiple fractures and pores are predominantly located near the altered zones. A weighted mean age of 15.9 ± 1.4 Ma (MSWD = 1.9, n = 4, UNTE1-A) was calculated for the patchy core, which has relatively low Th and higher U contents (~Th/U ratio of 45; Figs. 5d and f). Domain UNTE1- B displaying oscillatory zoning has a higher Th/U ratio of ~278 and a weighted mean age defining a fast-growth episode at 15.13 ± 0.36 Ma (MSWD = 3.7, n = 12). The altered UNTE1-D rim domain follows the same chemical trend of UNTE1- B and provides a younger age of 13.22 ± 0.95 Ma (MSWD = 3.7, n = 4). Spot 6 displaying a high uncertainty and was not considered (Table 3).

CAVR1 monazite (Figs. 5g-i) contains in its core mineral inclusions (plagioclase, adularia, chlorite and biotite) that are surrounded by a network of fractures (Fig. 5h). The oldest ages obtained are from one extremity of the grain (CAVR1-A) and range from 20.18 ± 0.64 to 15.51 ± 0.43 Ma (Fig. 5i); this lighter colored part may correspond to the starting point of the crystal growth, which was later partially dissolved (dissolution front). Scattered ages were also obtained from the central part of the grain close to the inclusions (CAVR1-B). CAVR1-C is chemically homogenous (Th/U ~160) providing an age of 13.87 ± 0.43 Ma (MSWD = 3.0, n = 10). CAVR1-D domain is very rich in Th (up to 204,961 ppm) and records a similar age of 13.90 ± 0.31 Ma (MSWD = 1.14, n = 3; Fig. 5i). Spots 26 and 27 are affected by cracks, showing particularly young dates and were excluded from the age range (Table 3).

GOTT1 monazite (Figs. 5j-l) is a fractured grain containing inclusions of plagioclase and biotite in its center. Two distinct chemical trends, GOTT1-A and GOTT1-B, are identified on the Th as function of U plot (Fig.5j) with average Th/U ratios of 56 and 19 respectively. The growth ages of the two domains cannot be discriminated, domain GOTT1-A recording an average age of 14.02 ± 0.44 Ma (MSWD = 2.6, n = 10) and GOTT1-B providing an age of 13.14 ± 0.69 Ma (MSWD = 8.5, n = 9) but shows more scattered single dates. Spot 11 providing a particularly old date with a high sigma value was not considered (Table 3).

Across the entire data set, monazite spot ages from this study record a crystallization duration of up to 10 Ma.

5. Discussion

Thorium-Pb dating of hydrothermal monazite is a robust method, Pb diffusion being negligible and the isotopic system being reset by dissolution/reprecipitation cycles (see above). High Pb_c contents were however observed for several analyses, suggesting the

presence of some remnants of not entirely dissolved older monazite during the dissolution-reprecipitation process (nanoscale remnants) or inclusions of other Th-U-Pb bearing minerals like thorite (e.g., Grand'Homme et al., 2016b). Hydrothermal monazite therefore typically displays high Th/U ratios at extremely low U contents. As the ^{232}Th-^{208}Pb isotopic system is not only the least affected by disturbance, but yields in the studied samples the most precise ages due to high Th contents compared to U.

The presented Th-Pb monazite ages cover a considerable period of time from circa 20 to 7 Ma (Figs. 4, 5 and 6, Tables 3 and 4). With the knowledge that monazite in fissures grows in response to fluid/rock interaction and that each deformation of the fissure induces chemical disequilibrium triggering a dissolution-precipitation cycle, these ages can be used to constrain the age of known deformation phases linked to specific tectonic events in the AM and GN, and to identify period of deformation that were previously undocumented in the study area.

5.1. The Gotthard nappe

The oldest ages obtained in this study are found in the GN, where almost all analyzed monazites come from horizontal fissures located in host rocks that display a steep foliation and lineation (Table 2). However, some fissures in the southern part of the GN dip to the south-east as folds developed during the formation of the Northern Steep Belt (NSB; Klaper, 1985; Milnes, 1974; Wiederkehr et al., 2008, 2009). The folding phase related to the development of the NSB is called Chièra phase in the eastern part of the GN, and occurred after 15.5 Ma based on Ar-Ar dating of biotite (e.g. Wiederkehr et al. 2009). The oldest monazite crystallization ages are recorded by growth domains in the BLAUBERG monazite dated by Janots et al. (2012); 15.5 ± 0.2 Ma, 15.2 ± 0.3 Ma, Fig. 6), UNTE1 monazite (15.9 ± 1.4 Ma, 15.13 ± 0.36 Ma, Figs. 5f, 6) and some individual Th-Pb dates in MUTT1, GOTT1, CAVR1 and SALZ2 (Figs. 5, 6). However, the main crystallization of monazite occurred in

the GN between 14 and 13 Ma (Fig. 6) and is consistent with the monazite age related to late tectonic activity in the Urseren zone (13.6 ± 1.5 Ma; Janots and Rubatto (2014). Biotite ages of Wiederkehr et al. (2009) were interpreted as recrystallization ages during Chièra phase deformation following the metamorphic peak at ~18 Ma in this area. We propose that the pronounced major fissure monazite crystallization (Fig. 6) in the GN is dating the main folding during the Chièra phase. The complete deformation history may have lasted longer and shows a general younging to the west (Wiederkehr et al., 2009).

In the south-western border of the GN, KLEM1 (8.43 ± 0.20 Ma) and BETT11 (9.96 ± 0.30 Ma and 7.53 ± 0.31 Ma) samples from Bergemann (2017) provide younger growth domain ages which are comparable in time to deformation recorded in the AM. We speculate that the fissures were probably tectonically overprinted and experienced monazite (re-)crystallization under transpressive conditions during the Oberaar and/or Rhone-Simplon phases (Fig. 6). Fault gouge K-Ar ages of illite from the Fadio-Bodio transect (south of the GN) provide a similar age range of 9.5 ± 0.2 - 7.1 ± 0.2 Ma (Zwingmann et al., 2010).

5.2. The Aar Massif

5.2.1. Overview and early fissures

Two fissure orientations are found in the AM and many of the older, horizontal fissures, were overprinted during younger deformation phases (e.g. Bergemann et al., 2017; Fig. 3b). In the northern part of the AM, fissures are horizontal and related to a steep foliation and down-dip lineation (e.g. Wehrens et al., 2017), reflecting the steep reverse faulting that affected the area between 22-11.5 Ma (Bergemann et al., 2017; Wehrens et al., 2017, Table 1). This early period of monazite growth corresponds to the Handegg phase of Wehrens et al. (2017) and a growth within the same age range is recorded in the north-eastern part of the AM in the Griesserental grain at 14.7 ± 0.5 Ma and 13.8 ± 0.2 Ma; (Janots et al., 2012) and in the

NEAT1 monazite (12.5 ± 1.2 to 12.1 ± 1.0 Ma, this study). Two additional grains from the same Griesserental fissure (Janots et al., 2012) provide average ages around 12-13 Ma (12.77 ± 0.09 Ma and 12.59 ± 0.18 Ma, Table A.1). Griesserental and NEAT1 main ages are equivalent to fault gouge K-Ar ages from Pleuger et al., (2012) and Griesserental monazite dates older than ~14 Ma overlap with ZFT.

In the central AM, K-Ar fault gouge ages from the Grimsel area are comprised between ~14 – 6 Ma and are in the same age range of monazite crystallization ages (Kralik et al., 1992; Pleuger et al., 2012; Fig. 6).

5.2.2. Strike slip movements

In the Grimsel area, strike-slip movements are recorded between ~ 12-11 Ma (Bergemann et al., 2017, Fig. 6; = Oberaar phase). Given that GRIM3 and GRIM4 monazite were found in vertical fissures, Bergemann et al. (2017) concluded that the transition from reverse faulting to dextral shearing occurred around 11.5 Ma (Fig. 6). In the Grimsel area, the strike-slip movements of the Oberaar phase overprint the horizontal fissures of the Handegg phase (PK2) and also lead to the formation of vertical fissures (GRIM3, 4; Bergemann et al., 2017). The texture of monazite PK2 reported by Bergemann et al., (2017) does not display any clear signs of dissolution/reprecipitation episodes, indicating that only monazite related to the Oberaar phase crystallized in these horizontal fissures. Grain GAST1 from this study records domain ages of 11.15 ± 0.61 Ma and younger indicating that tectonic movements coeval with the Oberaar phase after 11.5 Ma also occurred in the northern edge of the Aar Massif (see discussion below).

In the southwestern and central part of the AM, vertical fissures associated to steep foliation and flat lineation were formed in reaction to strike-slip movements related to the Rhone-Simplon phase (Bergemann et al., 2017; Berger et al., 2013). Younger ages dating strike-slip

deformation of the Rhone-Simplon line, recorded by fissure monazite, are provided by multiple samples that yield ages from ~9-6 Ma (Fig. 6). Similar young ages are also observed in the Aiguilles Rouges and Mont Blanc area (Bergemann et al., 2019). The time constraints provided by the monazite for this deformation phase are ~2 Ma younger than constraints given by Campani et al. (2010) based on Ar-Ar crystallization ages of white mica (Table 1).

5.2.3. The Pfaffenchopf thrusting

The Pfaffenchopf deformation phase is characterised by a flat-lying NW directed horizontal thrust that affected the northern boundary of the AM overprinting the Handegg phase structures (e.g. Mair et al., 2018, Berger et al., 2017, Wehrens et al., 2017; Fig. 1). Although monazite GAST1 was found in a block at the foot of a wall, its position suggests that crystallization occurred during the Pfaffenchopf phase (Fig. 6) and possibly later. For this reason, we interpret crystallization of GAST1 to constrain the Pfaffenchopf phase to 11.15 ± 0.61 Ma. The younger growth domain age in GAST1 indicates either that the Pfaffenchopf phase lasted until 9.4 ± 1.2 Ma or that strike-slip movements coeval with the Rhone-Simplon and Oberaar deformation phases also affect the northern limit of the Aar Massif.

Comparable spot ages obtained in samples further to the NE (SALZ21, GUTT1 and GOSCH1) may be linked to the Oberaar phase or to the coeval Pfaffenchopf deformation phase (Herwegh et al. 2015, Berger et al. 2017). In these cases, we do not have additional field evidence to link the ages with one of the two deformation phases.

5.2.4. Late thrust reactivation

Sample NEAT1 was taken from a fissure near a fault zone beneath the locality Herrenlimi, Etzlital, in the NEAT Tunnel (Fig. 1), located at the boundary of Permo-Carboniferous rocks with the crystalline basement. Mesozoic mylonitic carbonates occurring in same fault zone (at

the eastern end of the Maderanertal) mark the foot thrust of the Windgällen fold (Berger et al., 2016). This major fault zone is connected to the Färnigen zone (= Windgällen-Färnigen Zone) and its formation predates the steep movements of the Handegg deformation phase (Nibourel et al., 2018). The monazite NEAT1 shows growth stages at ~12 Ma and partial recrystallization until ~7 Ma (Figs. 4c and 6). Based on the overprint relationships the Windgällen basal thrust is as old as 22 Ma (Nibourel et al., 2018). The measured monazites provide the first evidence that this fault zone was reactivated during younger deformation stages. The main age of ~12 Ma is equivalent to fault gouge data from Pleuger et al., (2012) from this area and may be related to reverse faulting or early strike-slip faulting. In this area, horizontal lineation locally exists in the fault zone, indicating strike-slip movements (L. Nibourel, pers comm. 2018). The youngest date recorded by monazite around 7 Ma is as young as the AFT ages in the area (e.g., sample MRP247, MRP248, CGP21 and 115900; Glotzbach et al., 2009; Weisenberger et al., 2012; Fig. 7).

5.3. The link of fissures and temperature evolution

As detailed in the introduction, the development of fissures and the related hydrodynamics may be multiphase and include different aspects (e.g., change in fluid chemistry, different dynamics of fluid/host-rock interaction, etc.). Hydrothermal monazite typically crystallizes in the temperature range covered by zircon fission track (ZFT) and zircon (U-Th)/He thermochronometers, i.e. between a maximum of 380 - 190 °C and a minimum of 220 - 150 °C (Fig. 6; Bergemann et al., 2017, 2018; Glotzbach et al., 2010; Gnos et al., 2015; Reiners, 2005). Apatite fission track ages (AFT, partial annealing zone in the range of ~120 - 60 °C, Glotzbach et al., 2010) also tend to overlap with or postdate monazite growth suggesting that monazite crystallization occurs near to or above apatite closure temperature (Fig. 6). White mica Ar-Ar crystallization ages (growing syn-kinematically at ~400 - 350°C; Rolland et al.,

2009) tend to predate monazite growth in the central and south-western AM (Fig. 6; Pleuger et al., 2012). Fissure monazite ages also overlap with K-Ar ages from muscovite/illite crystallization in fault gouges recorded in the central and north-eastern part of the AM (~250 - 70°C, Pleuger et al., 2012; Fig. 6). Ar-Ar data on adularia from fault breccia yield distinctly younger crystallization ages of 3.30 ± 0.06 Ma. We speculate that this youngest phase of deformation, so far only reported from fault breccia from the Grimsel area, was likely not recorded by monazite due to the too low temperatures of the environment (160-100°C; Fig. 6; Hofmann et al., 2004; Pleuger et al., 2012).

Th-Pb dating of hydrothermal fissure monazite has proven to be a reliable method for studying deformation activity at lower greenschist to sub-greenschist facies conditions (Bergemann et al., 2017, 2018; Berger et al., 2013; Gasquet et al., 2010; Gnos et al., 2015; Grand'Homme et al., 2016a; Janots et al., 2012). The dataset from the AM and GN supports previous monazite dating and are complementary to available thermochronological data.

6. Summary and conclusion

The combination of fissure monazite age groups and structural observations allows detailed insights into the timing of orogenic processes. In contrast to syn-kinematically grown micas, commonly used for dating high strain zones, fissure monazite records also minor deformation causing changes in the fluid dynamics inside fissures. The ages, which can be connected to deformation phases, may indicate a change in the prevailing stress field during fissure formation.

The oldest deformation, which produces monazites in open fissures is related to reverse faulting during the Handegg phase in the AM (Berger et al., 2017; Wehrens et al., 2017). This is recorded by monazites from the Griesserental (~15-12.5 Ma, Janots et al., 2012), the Gotthard Base Tunnel (NEAT1: 12.5-12.1 Ma) and probably north of the Grimsel area

(GUTT1: ~14 Ma). In the AM, these data are time equivalent to the Handegg deformation and coeval deformation in the GN (domains in UNTE1 of 15.9 ± 1.4 and 15.13 ± 0.36 Ma). In the GN, a pronounced deformation phase is well defined by fissure monazite between ~ 14-13 Ma (MUTT1, CAVR1, GOTT1, BLAS1, UNTE1, DUTH2, SALZ2, BLAUBERG) and is interpreted as deformation caused by backfolding (Chièra phase) along the NSB. In the northern border of the AM, we interpret crystallization of GAST1 to constrain the Pfaffenchopf thrusting at 11.15 ± 0.61 Ma and that this deformation phase lasted possibly until 9.4 ± 1.2 Ma or that strike-slip movements subsequently affected this area. In the Grimsel area, early dextral strike-slip movements are recorded between ~12-11 Ma (Bergemann et al., 2017, Oberaar phase). Monazite ages dating dextral strike-slip movements at ~ 9-6 Ma are abundant in the southwestern AM and are also present in the Grimsel area. Therefore, Rhone Simplon and Oberaar strike slip movements are probably connected to each other and related to a similar stress field causing lateral escape movements. Some fissures also record monazite growth in a time interval for which field evidence for strike-slip movements is weak or absent (e.g., NEAT1, GUTT1).

Our study confirms that Th-Pb dating of hydrothermal fissure monazite is a reliable, complementary method for studying shear zone activity at greenschist to sub-greenschist facies conditions. Monazite crystallization ages coincide with K-Ar crystallization ages of muscovite/illite from fault gouges and are also consistent with the thermochronological record. Combination of Th-Pb data acquired on hydrothermal monazite grains from this and earlier reveal that stepwise growth (and dissolution/reprecipitation) of fissure monazite occurred over a time range of at least 10 Ma in the AM and GN. The new data allow to confirm, or to better delimit the age and duration of the previously defined successive deformation phases, and in some areas also to postulate hitherto unrecognized fault activity.

Acknowledgments

We would like to thank Peter Amacher, Paul Bähler, Rudolf Duthaler, Michael Flepp, Leo Klemm, Kurt Koch, Alexandre Salzmann and Josef Zurfluh for having provided monazites for this study. We thank Emilie Janots for the helpful discussions, Anne-Sophie Bouvier for technical support at the SwissSIMS facility and Agathe Martignier for technical assistance at the SEM. This study was financially supported by the SNF grant number 200020-165513. The Nordsim ion microprobe is operated by the research funding agencies of Denmark, Iceland, Norway, and Sweden, the Geological Survey of Finland, and the Swedish Museum of Natural History.

References

Aleinikoff, J.N., Schenck, W.S., Plank, M.O., Srogi, L.A., Fanning, C.M., Kamo, S.L., Bosbyshell, H., 2006. Deciphering igneous and metamorphic events in high-grade rocks of the Wilmington complex, Delaware: Morphology, cathodoluminescence and backscattered electron zoning, and SHRIMP U-Pb geochronology of zircon and monazite. Bull. Geol. Soc. Am. 118, 39–64. https://doi.org/10.1130/B25659.1

Bergemann, C.A., 2017. Crystallization age of Alpine cleft monazite-(Ce) and correlation with tectonically driven hydrothermal dissolution / precipitation events. PhD-thesis. University of Geneva.

Bergemann, C.A., Gnos, E., Berger, A., Janots, E., Whitehouse, M.J., 2019a. Constraining metamorphic dome exhumation and fault activity through hydrothermal monazite-(Ce) 1–23.

Bergemann, C.A., Gnos, E., Berger, A., Whitehouse, M., Mullis, J., Wehrens, P., Pettke, T., Janots, E., 2017. Th-Pb ion probe dating of zoned hydrothermal monazite and its implications for repeated shear zone activity: An example from the central alps,

Switzerland. Tectonics 36, 671–689. https://doi.org/10.1002/2016TC004407

Bergemann, C.A., Gnos, E., Berger, A., Whitehouse, M.J., Mullis, J., Walter, F., Bojar, H.-P., 2018. Constraining long-term fault activity in the brittle domain through in situ dating of hydrothermal monazite. Terra Nov. 30, 440–446. https://doi.org/10.1111/ter.12360

Bergemann, C.A., Gnos, E., Whitehouse, M.J., 2019b. Insights into the tectonic history of the Western Alps through dating of fi ssure monazite in the Mont Blanc and Aiguilles Rouges Massifs. Tectonophysics 750, 203–212. https://doi.org/10.1016/j.tecto.2018.11.013

Berger, A., Gnos, E., Janots, E., Whitehouse, M., Soom, M., Frei, R., Waight, T.E., 2013. Dating brittle tectonic movements with cleft monazite: Fluid-rock interaction and formation of REE minerals. Tectonics 32, 1176–1189. https://doi.org/10.1002/tect.20071

Berger, A., Mercolli, I., Herwegh, M., Gnos, E., 2017. Explanatory Notes to the Geological map of the Aar Massif, Tavetsch and Gotthard Nappes, Geological Special Map 1 : 100000. Federal Office of Topography Swisstopo, Wabern.

Berger, A., Mercolli, I., Herwegh, M., Gnos, E., 2016. Geological Map of the Aar Massif, Tavetsch and Gotthard Nappes.

Bousquet, R., Oberhänsli, R., Schmid, S.., Berger, A., Wiederkehr, M., Robert, C., Möller, A., Rosenberg, C., Zeilinger, G., Molli, G., Koller, F., 2012. Metamorphic framework of the Alps: Map 1: 1 000 000., University of Basel.

Campani, M., Mancktelow, N., Seward, D., Rolland, Y., Müller, W., Guerra, I., 2010. Geochronological evidence for continuous exhumation through the ductile-brittle transition along a crustal-scale low-angle normal fault: Simplon Fault Zone, central Alps. Tectonics 29, TC3002. https://doi.org/10.1029/2009TC002582

Cherniak, D.J., Pyle, J.M., 2008. Th diffusion in monazite. Chem. Geol. 256, 52–61. https://doi.org/10.1016/j.chemgeo.2008.07.024

Cherniak, D.J., Watson, E.B., Grove, M., Harrison, T.M., 2004. Pb diffusion in monazite: A combined RBS/SIMS study. Geochim. Cosmochim. Acta 68, 829–840. https://doi.org/10.1016/j.gca.2003.07.012

Cox, S.F., 2010. The application of failure mode diagrams for exploring the roles of fluid pressure and stress states in controlling styles of fracture-controlled permeability enhancement in faults and shear zones. Geofluids 217–233. https://doi.org/10.1111/j.1468-8123.2010.00281.x

Ford, M., Duchêne, S., Gasquet, D., Vanderhaeghe, O., 2006. Two-phase orogenic convergence in the external and internal SW Alps. J. Geol. Soc. London. 163, 815–826. https://doi.org/10.1144/0016-76492005-034

Gasquet, D., Bertrand, J.M., Paquette, J.L., Lehmann, J., Ratzov, G., Ascenção De Guedes, R.A., Tiepolo, M., Boullier, A.M., Scaillet, S., Nomade, S., 2010. Miocene to Messinian deformation and hydrothermal activity in a pre-Alpine basement massif of the French western Alps: New U-Th-Pb and argon ages from the Lauzière massif. Bull. la Soc. Geol. Fr. 181, 227–241. https://doi.org/10.2113/gssgfbull.181.3.227

Glotzbach, C., Reinecker, J., Danišík, M., Rahn, M., Frisch, W., Spiegel, C., 2010. Thermal history of the central Gotthard and Aar massifs, European Alps: Evidence for steady state, long-term exhumation. J. Geophys. Res. Earth Surf. 115, F03017. https://doi.org/10.1029/2009JF001304

Glotzbach, C., Spiegel, C., Reinecker, J., Rahn, M., Frisch, W., 2009. What perturbs isotherms? An assessment using fission-track thermochronology and thermal modelling along the Gotthard transect, Central Alps. Geol. Soc. London, Spec. Publ. 324 (1), 111–124.

Gnos, E., Janots, E., Berger, A., Whitehouse, M., Walter, F., Pettke, T., Bergemann, C., 2015. Age of cleft monazites in the eastern Tauern Window: constraints on crystallization

conditions of hydrothermal monazite. Swiss J. Geosci. 108, 55–74. https://doi.org/10.1007/s00015-015-0178-z

Grand'Homme, A., Janots, E., Bosse, V., Seydoux-Guillaume, A.M., Ascenção De Guedes, R.A., 2016a. Interpretation of U-Th-Pb in-situ ages of hydrothermal monazite-(Ce) and xenotime-(Y): evidence from a large-scale regional study in clefts from the western alps. Mineral. Petrol. 110, 787–807. https://doi.org/10.1007/s00710-016-0451-5

Grand'Homme, A., Janots, E., Seydoux-Guillaume, A.M., Guillaume, D., Bosse, V., Magnin, V., 2016b. Partial resetting of the U-Th-Pb systems in experimentally altered monazite: Nanoscale evidence of incomplete replacement. Geology 44, 431–434. https://doi.org/10.1130/G37770.1

Grand'Homme, A., Janots, E., Seydoux-Guillaume, A.M., Guillaume, D., Magnin, V., Hövelmann, J., Höschen, C., Boiron, M.C., 2018. Mass transport and fractionation during monazite alteration by anisotropic replacement. Chem. Geol. 484, 51–68. https://doi.org/10.1016/j.chemgeo.2017.10.008

Heijboer, T.C., 2006. Origin and pathways of pro- and retro- grade fluids, PTt paths and fluid-mineral equilibria from Alpine veins of the Central Alps: Case studies of the Fibbia and Amsteg areas. PhD-thesis.

Herwegh, M., Berger, A., Baumberger, R., Wehrens, P., Kissling, E., 2017. Large-Scale Crustal-Block-Extrusion During Late Alpine Collision. Sci. Rep. 7, 1–10. https://doi.org/10.1038/s41598-017-00440-0

Hofmann, B. a, Helfer, M., Diamond, L.W., Villa, I.M., Frei, R., Eikenberg, J., 2004. Topography-driven hydrothermal breccia mineralization of Pliocene age at Grimsel Pass, Aar massif, Central Swiss Alps. Schweizerische Mineral. Und Petrogr. Mitteilungen 84, 271–302. https://doi.org/10.5169/seals-63750

Janots, E., Berger, A., Gnos, E., Whitehouse, M., Lewin, E., Pettke, T., 2012. Constraints on

fluid evolution during metamorphism from U–Th–Pb systematics in Alpine hydrothermal monazite. Chem. Geol. 326, 61–71.

Janots, E., Rubatto, D., 2014. U-Th-Pb dating of collision in the external Alpine domains (Urseren zone, Switzerland) using low temperature allanite and monazite. Lithos 184–187, 155–166. https://doi.org/10.1016/j.lithos.2013.10.036

Klaper, E.M., 1985. Deformation history and metamorphic mineral growth along the Pennine frontal thrust (Wallis/Ticino). PhD-thesis. ETH Zürich.

Kralik, M., ClauerLAUER, N., Holnsteiner, R., Huemer, H., Kappel, F., 1992. Recurrent fault activity in the Grimsel Test Site (GTS, Switzerland): revealed by Rb-Sr, K-Ar and tritium isotope techniques. J. Geol. Soc. London. 149, 293–301. https://doi.org/10.1144/gsjgs.149.2.0293

Ludwig, K.R., 2009. Squid2: a user manual. Berkeley Geochronol. Cent. Spec. Publ. 5, 1–110.

Ludwig, K.R., 2003. User's manual for a geochronological toolkit for Microsoft Excel (Isoplot/Ex version 3.0). Berkeley Geochronol. Cent. Spec. Publ. 4, 1–70.

Mair, D., Lechmann, A., Herwegh, M., Nibourel, L., Schlunegger, F., 2018. Linking Alpine deformation in the Aar Massif basement and its cover units – the case of the Jungfrau-Eiger Mountains (Central Alps, Switzerland). Solid Earth Discuss. 1–38. https://doi.org/10.5194/se-2018-49

Meldrum, A., Boatner, L.A., Weber, W.J., Ewing, R.C., 1998. Radiation damage in zircon and monazite. Geochim. Cosmochim. Acta 62, 2509–2520. https://doi.org/10.1016/S0016-7037(98)00174-4

Mercolli, I., Schenker, F., Stalder, H.A., 1984. Geochemie der Veränderungen von Granit durch hydrothermale Lösungen (Zentraler Aaregranit). Schweizerische Mineral. und Petrogr. Mitteilungen 64. 1-2, 67–82.

Michalski, I., Soom, M., 1990. The Alpine thermo-tectonic evolution of the Aar and Gotthard massifs, Central Switzerland - Fission Track ages on zircon and apatite and K-Ar mica ages. Schweiz. Miner. Petrogr. Mitteilg 70, 373–387. https://doi.org/10.5169/seals-53628

Milnes, A.G., 1976. Strukturelle Probleme im Bereich der Schweizer Geotraverse–das Lukmanier- Massiv. Schweizerische Mineral. und Petrogr. Mitteilungen 56 56, 615–618.

Milnes, A.G., 1974. Structure of the Pennine Zone (Central Alps): A New Working Hypothesis. GSA Bull. 85 (11), 1727–1732.

Mullis, J., 1996. P-T-t path of quartz formation in extensional veins of the Central Alps P-T-t path of quartz formation in extensional veins of the Central Alps *. Schweiz. Miner. petrogr. mitt. 76, 159–164. https://doi.org/10.5169/seals-57694

Nibourel, L., Berger, A., Egli, D., Luensdorf, N.K., Herwegh, M., 2018. Large vertical displacements of a crystalline massif recorded by Raman thermometry. Geology 46, 879–882. https://doi.org/10.1130/G45121.1

Pleuger, J., Mancktelow, N., Zwingmann, H., Manser, M., 2012. K-Ar dating of synkinematic clay gouges from Neoalpine faults of the Central, Western and Eastern Alps. Tectonophysics 550–553, 1–16. https://doi.org/10.1016/j.tecto.2012.05.001

Reinecker, J., Danišík, M., Schmid, C., Glotzbach, C., Rahn, M., Frisch, W., Spiegel, C., 2008. Tectonic control on the late stage exhumation of the Aar Massif (Switzerland): Constraints from apatite fission track and (U-Th)/He data. Tectonics 27, TC6009. https://doi.org/10.1029/2007TC002247

Reiners, P.W., 2005. Zircon (U-Th)/He thermochronometry. Rev. Mineral. Geochemistry 58.1, 151–179.

Rolland, Y., Cox, S.F., Corsini, M., 2009. Constraining deformation stages in brittle-ductile shear zones from combined field mapping and40Ar/39Ar dating: The structural evolution of the Grimsel Pass area (Aar Massif, Swiss Alps). J. Struct. Geol. 31, 1377–

1394. https://doi.org/10.1016/j.jsg.2009.08.003

Rolland, Y., Rossi, M., Cox, S.F., Corsini, M., Mancktelow, N., Pennacchioni, G., Fornari, M., Boullier, A.M., 2008. 40 Ar/ 39 Ar dating of synkinematic white mica: insights from fluid-rock reaction in low-grade shear zones (Mont Blanc Massif) and constraints on timing of deformation in the NW external Alps. Geol. Soc. London, Spec. Publ. 299, 293–315. https://doi.org/10.1144/sp299.18

Rossi, M., Rolland, Y., 2014. Stable isotope and Ar/Ar evidence of prolonged multiscale fluid flow during exhumation of orogenic crust: Example from the mont blanc and Aar Massifs (NW Alps). Tectonics 33, 1681–1709. https://doi.org/10.1002/2013TC003438

Schaer, J.P., Reimer, G.M., Wagner, G.A., 1975. Actual and ancient uplift rate in the Gotthard region, Swiss Alps: a comparison between precise levelling and fission-track apatite age. Dev. Geotecton. Elsevier 9, 293–300.

Schmid, S.M., Fügenschuh, B., Kissling, E., Schuster, R., 2004. Tectonic map and overall architecture of the Alpine orogen. Eclogae Geol. Helv. 97, 93–117. https://doi.org/10.1007/s00015-004-1113-x

Seydoux-Guillaume, A.M., Bingen, B., Bosse, V., Janots, E., Laurent, A.T., 2018. Transmission Electron Microscope imaging sharpens geochronological interpretation of zircon and monazite. Microstruct. Geochronol. Planet. Rec. Down to Atom Scale 232, 261–275.

Seydoux-Guillaume, A.M., Goncalves, P., Wirth, R., Deutsch, A., 2003. Transmission electron microscope study of polyphase and discordant monazites: Site-specific specimen preparation using the focused ion beam technique. Geology 31, 973–976. https://doi.org/10.1130/G19582.1

Seydoux-Guillaume, A.M., Montel, J.M., Bingen, B., Bosse, V., de Parseval, P., Paquette, J.L., Janots, E., Wirth, R., 2012. Low-temperature alteration of monazite: Fluid mediated

coupled dissolution-precipitation, irradiation damage, and disturbance of the U-Pb and Th-Pb chronometers. Chem. Geol. 330–331, 140–158. https://doi.org/10.1016/j.chemgeo.2012.07.031

Seydoux-Guillaume, A.M., Paquette, J.L., Wiedenbeck, M., Montel, J.M., Heinrich, W., 2002. Experimental resetting of the U-Th-Pb systems in monazite. Chem. Geol. 191, 165–181. https://doi.org/10.1016/S0009-2541(02)00155-9

Stacey, J. S., and Kramers, J. D., 1975. Approximation of terrestrial lead isotope evolution by a two-staged model. Earth Planet. Sci. Lett. 26, 207–221.

Stalder, H.A., Wagner, A., Graeser, S., Stuker, P., 1998. Mineralienlexikon der Schweiz. Wepf, Basel.

Valla, P.G., Van Der Beek, P.A., Shuster, D.L., Braun, J., Herman, F., Tassan-Got, L., Gautheron, C., 2012. Late Neogene exhumation and relief development of the Aar and Aiguilles Rouges massifs (Swiss Alps) from low-temperature thermochronology modeling and $^{4}He/^{3}He$ thermochronometry. J. Geophys. Res. Earth Surf. 117, 1–23. https://doi.org/10.1029/2011JF002043

Vernon, A.J., Van Der Beek, P.A., Sinclair, H.D., Persano, C., Foeken, J., Stuart, F.M., 2009. Variable late Neogene exhumation of the central European Alps: Low-temperature thermochronology from the Aar Massif, Switzerland, and the Lepontine Dome, Italy. Tectonics 28, 1–21. https://doi.org/10.1029/2008TC002387

Wagner, G.A., 1977. Cooling ages derived by apatite fission-track, mica Rb-Sr and K-Ar dating; the uplift and cooling history of the Central Alps. Mem. Inst. Geol. Miner. Univ. Padova 30, 1–27.

Wehrens, P., Baumberger, R., Berger, A., Herwegh, M., 2017. How is strain localized in a meta-granitoid, mid-crustal basement section? Spatial distribution of deformation in the central Aar massif (Switzerland). J. Struct. Geol. 94, 47–67.

https://doi.org/10.1016/j.jsg.2016.11.004

Weisenberger, T.B., Rahn, M., van der Lelij, R., Spikings, R.A., Bucher, K., 2012. Timing of low-temperature mineral formation during exhumation and cooling in the Central Alps, Switzerland. Earth Planet. Sci. Lett. 327–328, 1–8. https://doi.org/10.1016/j.epsl.2012.01.007

Wiederkehr, M., Bousquet, R., Schmid, S.M., Berger, A., 2008. From subduction to collision: Thermal overprint of HP/LT meta-sediments in the north-eastern Lepontine Dome (Swiss Alps) and consequences regarding the tectono-metamorphic evolution of the Alpine orogenic wedge. Swiss J. Geosci. 101. https://doi.org/10.1007/s00015-008-1289-6

Wiederkehr, M., Sudo, M., Bousquet, R., Berger, A., Schmid, S.M., 2009. Alpine orogenic evolution from subduction to collisional thermal overprint: The $^{40}Ar/^{39}Ar$ age constraints from the Valaisan Ocean, central Alps. Tectonics 28. https://doi.org/10.1029/2009TC002496

Zwingmann, H., Mancktelow, N., Antognini, M., Lucchini, R., 2010. Dating of shallow faults: New constraints from the AlpTransit tunnel site (Switzerland). Geology 38, 487–490. https://doi.org/10.1130/G30785.1

Tables

Table 1. Summary of deformation phases in the Aar Massif and the Gotthard Nappe

Table 2. Summary of monazite samples considered in this study (samples location, host-rock, fissure mineralogy and orientation)

Table 3. Th-U-Pb analyses of monazite by ion microprobe (SwissSIMS)

Table 4. Th-U-Pb analyses of monazite by ion microprobe (Nordsim)

TableA.1. Supplementary Th-U-Pb analyses (Nordsim) of monazite from Griesserental fissure (Janots et al., 2012)

TableA.2. Supplementary electron microprobe analyses of monazite grains GOSCH1 and SALZ21

Figure captions

Fig. 1. Simplified geological map of the Aar Massif and the Gotthard Nappe. Older, horizontal fissures are marked by red stars and younger, vertical fissures by blue stars. Samples with unknown orientation were found in a block at the foot of a wall and are indicated by a grey star. Samples from this study are labelled in black, whereas samples analysed by Bergemann (2017), Bergemann et al., (2017), Berger et al., (2013) and Janots et al., (2012) are labelled in green. On the map, we indicate the weighted mean age or a range of weighted mean ages of the growth domains for each grain, except for GUTT1 where only the spot age range is indicated.

Fig. 3. Examples of fissures (subparallel walls) and clefts (outwards curved walls) in the Aar Massif and the Gotthard Nappe. Horizontal and vertical structures are depicted by red and blue dashed lines respectively. a) 25 cm long, vertical fissure in aplitic band at Oberaargletscher, Grimsel Pass region, Aar Massif, described in Bergemann et al., (2017). b) Vertical fissure crosscutting an older horizontal fissure at Kleines Wannenhorn, Fieschertal, Aar Massif (photo: Thilo Arlt). The metal stick is 50 cm long. c) Several meter large fissure in granodiorite with nicely visible dissolution (bleached) zone, Grimsel Pass region, Aar Massif. d) Horizontal cleft in granitic gneiss with curved walls, Gotthard road tunnel, Gotthard Nappe. The cleft is 50 cm in size.

Fig. 2. Summary sketch of the tectonic evolution and fissure orientation in the Aar Massif and Gotthard Nappe, showing the deformation phases discussed in this paper. Modified from Herwegh et al. (2017).

Fig. 4. Th versus U plots (left), BSE images (centre) and weighted average ages (right) of monazite grains from the Aar Massif analysed by ion microprobe.

Fig. 5. Th versus U plots (left), BSE images (centre) and weighted average ages (right) of monazite grains from the Gotthard Nappe analysed by ion microprobe.

Fig. 6. Summary of Th-Pb crystallization ages of fissure monazite from the Aar Massif and the Gotthard Nappe (samples from this study are labeled black; samples from Bergemann, 2017; Bergemann et al., 2017; Berger et al., 2013; Janots et al., 2012 are labeled green) compared to other crystallization and cooling ages from Ar-Ar adularia: Hofmann et al., (2004); K-Ar from fault gouges: Pleuger et al., (2012), Kralik et al., (1992); Ar-Ar white mica: Campani et al., (2010); Rolland et al., (2009); Zircon (U-Th)/He: Glotzbach et al., (2010); ZFT: Berger et al., (2017); Glotzbach et al., (2010); Michalski and Soom, (1990); Pleuger et al., (2012); AFT: Berger et al., (2017); Glotzbach et al., (2010), (2009); Michalski and Soom, (1990); Pleuger et al., (2012); Reinecker et al., (2008); Schaer et al., (1975); Wagner, (1977); Weisenberger et al., (2012). Red spots indicate age results obtained on monazites from horizontal fissures (in the Gotthard Nappe also including inclined fissures) and blue spots indicate monazite ages obtained from vertical fissures. Grey bars indicate the range of the dates in each sample, whereas filled dots with error bars indicate growth domains constrained by averaging multiple dates. Age ranges of deformation phases are indicated to the left and to the right of the diagrams. Solid bars indicate age range constrained in this study and dashed lines indicate age range provided by others (see Table 1). The colored horizontal bars indicate the monazite crystallization age range obtained during this study. Note that in some horizontal fissure monazite growth only occurs during a younger deformation stage during which newly formed fissures are vertical in orientation. Note also that the begin of the Handegg and Chièra phases cannot be constrained with fissure monazite because they start at P-T conditions where fissure monazite was not stable and/or the fissure had not yet formed. Notably, in the Gotthard Nappe the cluster of monazite ages is indicating that the Chièra backfolding phase is younger than previously reported.

Fig. 7. Time-temperature diagram for crystallization ages of fissure monazite compared to ZFT and AFT from the north-eastern part of the Aar Massif. Data for Griesserental are from Janots et al., (2012) and NEAT1 ages are from this study.

Table 1. Summary of deformation phases in the Aar Massif and the Gotthard Nappe

	Age [Ma]	Phase	Domain	Characteristics	Monazite age [Ma]	Ref.	Remarks
1	**31 - 28**	D2	Gotthard Nappe	nappe stacking		F	
2	**30 - 22**	Kiental	West Helvetics	nappe stacking with folding		C	linked to 3
3	**30 - 22**	Calanda	East Helvetics	nappe stacking with folding		F	linked to 2
4	**22 - 11.5**	Handegg	Aar Massif	reverse faults		I	
5	**11.5 - 7**	Oberaar	Southern Aar Massif	strike slip	12 - 11	A, I	
6	**12 - 5(?)**	Pfaffenchopf	Northern Aar Massif	flat-lying NW directed thrusting		I	
7	**20 - 15**	Chièra	Eastern Gotthard Nappe, NSB, Grava	large scale folding, producing NSB		J	must be linked to 4
8	**12 - 9**	Berisal	Western Gotthard Nappe	large scale folding, producing NSB		F	must be linked to 4
9	**14.2 - 11**	Rhone-Simplon	NSB, western Aar Massif	strike slip (normal faulting)	10 - 6	A, B, D	linked to 5

A: Bergemann 2017; Bergemann et al., 2017; B: Berger et al., 2013; C: Burkhard 1988; D: Campani et al. 2010; E: Challandes et al., 2008; F: Pfiffner 1977, 2014; G: Rolland et al., 2009; H: Rossi and Rolland, 2014; I: Wehrens et al. 2016, 2017; J: Wiederkehr et al. 2008, 2009. NSB = Northern Steep Belt (Milnes, 1974).

Table 2. Summary of monazite samples from the central Alps (Switzerland) considered in this study (samples location, host-rock, fissure mineralogy and orientation)

Locality	Sample	Latitude (°N)	Longitude (°E)	Host-rock	Alpine met.	Association	Ref.	Fissure orientation
Aar Massif								
Gotthard Base Tunnel, Unter Herrenlimi, Etzlital, Uri	NEAT1	46°45.049'	008°42.623'	sericite schist	LGS	Ab, Qz, Ilm, Ant, Clc	1	horizontal
Jolital, Valais	JOLI2	46°20.86'	007°48.14'	gneiss	LGS	Adl, Qz, Ant, Clc	1	Vertical, block in scree
Gasterntal, Bern	GAST1	46°26.63'	007°44.60'	gneiss	LGS	Ab, Qz, Ant, Clc	1	block fall at base of wall
Göscheneralp, Uri	GOSCH1	46°40.4'	008°25.1'	gneiss	UGS	Adl, Qz, Ant, Clc	1	horizontal
Guttannen, Bern	GUTT1	46°39.733'	008°17.083'	sericite gneiss	LGS	Ab, Adl, Qz, Ant, Cc, Brk, Clc, Ap	1	horizontal
Triftgletscher, Bern	SALZ21	46°40.5′	008°21.5′	gneiss	LGS	Adl, Chl, Ilm	1	horizontal
Grimsel, Bern	PK2	46°32.992'	008°16.233'	gneiss	LGS	Adl, Qz, Hem, Clc, Snt	2	horizontal
Grimsel, Bern	GRIM3	46°32.313'	008°13.904'	gneiss	LGS	Adl, Qz, Ilm, Clc	2	vertical
Grimsel, Bern	GRIM4	46°32.308'	008°13.874'	gneiss	LGS	Adl, Qz, Ilm, Clc	2	vertical

Baltschiedertal, Valais	BALT2	46°19.913'	007°52.533'	granite	LGS	Adl, Ab, Qz, Ilm, Ant, Clc, Ap, Xnt, Brt	3	vertical
Baltschiedertal, Valais	BALT4	46°19.913'	007°52.533'	granite	LGS	Adl, Ab, Qz, Ilm, Ant, Clc, Ap, Xnt, Brt	3	vertical
Griesserental, Uri	GRIESS.	46°45.56′	008°45.20′	gneiss	LGS	Ab, Adl, Qz, Ant, Ilm, Clc	4	horizontal
Gotthard Nappe								
Muttenhörner, Gerental (glacier NE of mountains), Uri	MUTT1	46°32.43'	008°26.71'	gneiss	UGS	Adl, Qz, Rt, Clc	1	horizontal
Sanktpeterstöckli, Unteralptal, Uri	UNTE1	46°35.280'	008°40.769'	gneiss	UGS	Adl, Qtz, Rt, Pyr, Clc	1	horizontal
Val Cavradi, Grison	CAVR1	46°38.258'	008°42.935'	sericite schist	LGS	Adl, Hem, Qz, Trm, Str	1	horizontal
Gotthard Road Tunnel, Uri	GOTT1	46°36.742'	008°35.632'	gneiss	UGS	Adl, Qtz, Clc, Xnt	1	horizontal
Piz Scai, Ticino	SALZ2	46°34.50'	008°45.75'	two-mica gneiss	UGS	Adl, Qz, Rt, Cc, Clc	2; 5	horizontal
Blauberg, Uri	BLAUBERG	46°34.57′	008°35.34′	two-mica gneiss	UGS	Adl, Qz, Hem, Ant, Cc, Clc	4	horizontal
Piz Blas, Val Nalps, Sedrun, Grisons	BLAS1	46°34.677’	008°43.980’	two-mica gneiss	UGS	Ab, Ad, Ilm, Cc	2; 5	inclined
Lago Sucro, Val Cadlimo, Tessin	DUTH2	46°33.8'	008°41.5'	gneiss	UGS	Qz, Ad, Ms,Bt, Chl, Ilm, Sdr, Pyr, Ap, Rt	2; 5	horizontal
Bettelbach, Niederwald,	BETT11	46°25.62'	008°11.70'	gneiss	UGS	Qtz, Adl, Ant, Rtl, Trm, Sd	2; 5	horizontal

Goms, Valais								
Grosses Arsch, Blinnental, Valais	KLEM1	46°26.7'	008°16.3'	gneiss	UGS	Qtz	2; 5	block fall at base of wall

Ab = albite; Adl =adularia; Ant = anatase; Ap = apatite; Brk = brookite; Cc =calcite; Chl =chlorite; Clc =clinochlore;Hem = hematite; Ilm = ilmenite; Pyr = pyrite; Qz = quartz; Snt = senaite; Sd = siderite; Str = strontianite; Trm = tourmaline; Xnt = xenotime. Alpine metamorphism: lower greenschist (LGS) and upper greenschist (UGS). References: 1: this study, 2: Bergemann et al. (2017), 3: Berger et al. (2013), 4: Janots et al. (2012), 5: Bergemann (2017).

Table 3. Th-U-Pb analyses of monazite by ion microprobe (SwissSIMS)

Aar Massif										207 - corr		208 - corr		207-corr spot ages		208-corr spot ages	
Groups	**Analysis ID**	**U (ppm)**	**Th (ppm)**	**Th/U**	**^{204}Pb/^{206}Pb**	**1σ (%)**	**^{208}Pb/^{206}Pb**	**1σ (%)**	**f208 (%)**	**^{208}Pb/^{232}Th**	**1σ (%)**	**^{206}Pb/^{238}U**	**1σ (%)**	**^{208}Pb/^{232}Th Age (Ma)**	**1σ (abs.)**	**^{206}Pb/^{238}U Age (Ma)**	**1σ (abs.)**
A	**Neat1@01**	34	27960	815	0.0389	11	35.5	13	4	0.000624	2.2	0.00193	2.4	12.61	0.28	12.46	0.30
	Neat1@02	35	29900	851	0.0472	12	47.0	12	4	0.000598	2.1	0.00186	2.2	12.09	0.25	11.96	0.27
	Neat1@03	35	26408	754	0.0413	13	43.4	11	4	0.000615	2.2	0.00191	2.4	12.43	0.28	12.28	0.29
	Neat1@04	46	35620	767	0.0475	11	43.9	11	4	0.000593	1.8	0.00184	2.0	11.98	0.22	11.82	0.24
	Neat1@05	36	28866	793	0.0408	12	41.4	12	4	0.000603	1.9	0.00187	2.0	12.18	0.23	12.01	0.24
B	**Neat1@06**	31	14318	463	0.0439	8.3	20.4	10	8	0.000638	2.1	0.00198	2.5	12.89	0.26	12.76	0.32
	Neat1@07	39	27037	687	0.0463	10	21.5	14	8	0.000574	3.8	0.00177	4.2	11.60	0.44	11.42	0.48
	Neat1@08	51	25199	493	0.0398	10	23.0	13	7	0.000646	2.9	0.00199	3.4	13.06	0.37	12.83	0.43
	Neat1@10	73	39247	538	0.0395	17	28.0	15	5	0.000574	3.8	0.00177	4.2	11.60	0.45	11.42	0.48
C	**Neat1@26**	12	11020	893	0.0422	12	22.7	11	7	0.000640	2.6	0.00200	3.0	12.93	0.33	12.86	0.38
	Neat1@27	38	28506	751	0.0497	15	29.4	12	7	0.000573	2.7	0.00177	3.0	11.59	0.32	11.42	0.35
	Neat1@28	20	18167	924	0.0415	13	17.9	11	9	0.000595	3.0	0.00184	3.6	12.03	0.36	11.85	0.43
	Neat1@30	17	13240	799	0.0461	15	31.8	10	6	0.000577	3.3	0.00178	3.5	11.65	0.38	11.44	0.40
D	**Neat1@16**	40	19911	496	0.0384	12	50.2	7.7	3	0.000584	1.9	0.00180	2.0	11.79	0.22	11.62	0.23
	Neat1@17	63	32430	514	0.0325	17	58.1	7.4	2	0.000521	2.0	0.00161	2.1	10.53	0.21	10.37	0.22
	Neat1@18	120	66365	554	0.0405	17	60.4	7.5	3	0.000403	1.9	0.00125	2.0	8.15	0.15	8.05	0.16
	Neat1@19	93	54534	589	0.0351	18	58.7	8.2	2	0.000419	2.2	0.00130	2.3	8.47	0.19	8.35	0.19
	Neat1@20	59	31622	537	0.0386	17	54.3	7.1	3	0.000478	3.1	0.00148	3.2	9.66	0.29	9.53	0.30
	Neat1@21	36	16083	442	0.0446	13	44.3	7.1	4	0.000562	2.1	0.00174	2.2	11.36	0.24	11.24	0.25
	Neat1@22	64	36915	573	0.0419	16	39.8	12	4	0.000453	2.2	0.00141	2.4	9.16	0.21	9.05	0.22
	Neat1@23	65	35134	544	0.0410	12	30.3	10	5	0.000473	2.7	0.00146	2.9	9.56	0.26	9.43	0.28
	Neat1@24	56	27605	489	0.0393	14	41.4	11	4	0.000521	2.4	0.00162	2.6	10.52	0.25	10.43	0.27

	Neat1@25	56	33326	592	0.0384	15	39.7	15	4	0.000530	2.5	0.00164	2.8	10.72	0.27	10.57	0.30
	Neat1@11	*23*	*9088*	*397*	*0.0404*	*7*	*7.7*	*13*	*20*	*0.000833*	*8.9*	*0.00263*	*12.7*	*16.82*	*1.49*	*16.95*	*2.15*
	Neat1@12	*20*	*8199*	*408*	*0.0412*	*9*	*9.7*	*14*	*16*	*0.000744*	*7.4*	*0.00232*	*9.5*	*15.04*	*1.12*	*14.95*	*1.41*
	Neat1@13	*29*	*13151*	*446*	*0.0437*	*9*	*10.0*	*14*	*17*	*0.000706*	*7.5*	*0.00220*	*9.7*	*14.26*	*1.07*	*14.16*	*1.37*
	Neat1@14	*43*	*17057*	*400*	*0.0392*	*9*	*8.3*	*15*	*18*	*0.000624*	*8.2*	*0.00192*	*11.2*	*12.62*	*1.04*	*12.40*	*1.39*
	Neat1@15	*122*	*46746*	*383*	*0.0451*	*23*	*45.2*	*3.9*	*4*	*0.000362*	*4.4*	*0.00112*	*4.6*	*7.32*	*0.32*	*7.20*	*0.33*
	Neat1@29	*62*	*53269*	*860*	*0.0401*	*16*	*26.5*	*13*	*6*	*0.000434*	*4.0*	*0.00133*	*4.5*	*8.76*	*0.35*	*8.59*	*0.39*
A	**Joli2@06**	15	3821	263	0.0157	22	8.39	4.7	7.2	0.000393	3.7	0.00099	4.9	7.94	0.29	6.38	0.31
	Joli2@07	27	4845	177	0.0185	22	11.6	6.8	6.2	0.000465	2.9	0.00131	4.2	9.39	0.27	8.45	0.35
	Joli2@08	43	2788	65	0.0218	20	7.70	8.2	11	0.000470	5.6	0.00133	8.5	9.51	0.53	8.59	0.73
	Joli2@10	52	3584	68	0.0208	24	9.97	5.0	8.1	0.000380	3.2	0.00108	4.5	7.68	0.24	6.97	0.32
	Joli2@11	89	4831	55	0.0238	23	8.55	6.9	11	0.000348	4.8	0.00100	7.7	7.04	0.34	6.42	0.49
	Joli2@12	97	2390	25	0.0304	14	3.67	1.9	32	0.000451	4.4	0.00130	11.0	9.11	0.40	8.37	0.92
B	**Joli2@01**	50	14663	294	0.0198	16	25.4	2.8	3.0	0.000422	2.2	0.00126	2.4	8.52	0.19	8.12	0.20
	Joli2@03	44	9303	211	0.0245	17	18.9	4.6	5.0	0.000381	2.1	0.00112	2.5	7.70	0.16	7.20	0.18
	Joli2@04	44	11587	263	0.0240	15	18.7	5.7	5.0	0.000406	2.3	0.00119	2.8	8.20	0.19	7.65	0.21
	Joli2@05	49	8539	174	0.0241	13	15.6	6.6	6.0	0.000436	2.4	0.00128	2.9	8.81	0.21	8.24	0.24
	Joli2@02	*95*	*30765*	*325*	*0.0192*	*21*	*20.6*	*5.6*	*3.6*	*0.000270*	*2.9*	*0.00080*	*3.2*	*5.46*	*0.16*	*5.14*	*0.16*
	Joli2@09	*45*	*1134*	*25*	*0.0279*	*18*	*3.6*	*8.2*	*30.1*	*0.000577*	*14.5*	*0.00161*	*35.9*	*11.65*	*1.69*	*10.35*	*3.72*
A	**Gast1@01**	52	3744	72	0.0254	15	10.2	8.8	9.6	0.000550	4.2	0.00169	6.5	11.12	0.47	10.87	0.70
	Gast1@03	116	7915	68	0.0221	24	6.88	14	12	0.000618	8.6	0.00181	13.2	12.49	1.07	11.66	1.54
	Gast1@04	56	3186	57	0.0312	21	7.47	8.5	16	0.000498	7.2	0.00151	11.6	10.07	0.73	9.72	1.13
	Gast1@05	63	5539	88	0.0344	16	9.63	10	14	0.000496	5.3	0.00150	7.7	10.02	0.53	9.66	0.74
	Gast1@06	19	1604	82	0.0403	14	6.45	11	24	0.000618	4.6	0.00183	6.1	12.48	0.58	11.76	0.71
	Gast1@07	52	5131	98	0.0325	16	8.42	12	15	0.000645	6.6	0.00194	9.6	13.03	0.85	12.51	1.20
	Gast1@08	40	4295	108	0.0311	20	10.6	11	11	0.000508	5.2	0.00152	7.0	10.27	0.53	9.81	0.69

	Gast1@12	40	3134	78	0.0297	19	9.58	8.7	12	0.000589	4.9	0.00176	6.7	11.89	0.58	11.35	0.76
	Gast1@13	60	4873	81	0.0323	19	9.50	9.3	13	0.000525	4.1	0.00158	6.0	10.61	0.44	10.18	0.61
	Gast1@17	29	4444	151	0.0485	11	6.12	7.0	31	0.000599	6.0	0.00186	9.3	12.10	0.72	11.97	1.11
	Gast1@18	24	3187	134	0.0424	10	5.19	7.8	32	0.000564	8.8	0.00179	15.0	11.41	1.00	11.55	1.73
	Gast1@21	63	8322	132	0.0395	18	6.17	10	25	0.000551	7.7	0.00166	11.7	11.14	0.85	10.71	1.25
B1	**Gast1@09**	61	12083	197	0.0353	20	17.9	11	7.6	0.000493	2.8	0.00149	3.5	9.97	0.28	9.61	0.33
B1	**Gast1@10**	68	12067	178	0.0268	23	17.4	11	6.0	0.000487	4.0	0.00148	4.9	9.84	0.39	9.56	0.47
B1	**Gast1@11**	78	11420	146	0.0337	18	14.7	12	8.9	0.000509	4.7	0.00153	5.6	10.28	0.48	9.83	0.55
B2	**Gast1@14**	406	19201	47	0.0129	19	9.22	4.0	5.4	0.000486	3.9	0.00143	5.1	9.82	0.38	9.23	0.48
B2	**Gast1@15**	317	13707	43	0.00643	54	8.61	4.4	2.9	0.000486	3.1	0.00145	5.1	9.83	0.31	9.33	0.48
B2	**Gast1@16**	453	21712	48	0.0179	17	8.57	5.1	8.1	0.000448	2.2	0.00132	4.0	9.04	0.20	8.49	0.34
	Gast1@02	*/*	*0*	*/*	*0.0391*	*15*	*7.46*	*8.5*	*20.2*	*0.000575*	*4.8*	*0.00175*	*7.3*	*11.62*	*0.56*	*11.24*	*0.82*

Gotthard nappe

A	**Mutt1@11**	45	8795	195	0.0274	16	17.0	12	6.2	0.000682	4.0	0.00210	4.8	13.79	0.55	13.49	0.64
A	**Mutt1@12**	54	6901	128	0.0359	13	12.4	11	11	0.000729	4.1	0.00224	5.3	14.73	0.61	14.43	0.76
A	**Mutt1@13**	64	7298	115	0.0361	11	10.8	11	13	0.000752	4.2	0.00229	5.5	15.19	0.63	14.72	0.82
A	**Mutt1@14**	81	16473	202	0.0409	15	15.6	15	10	0.000669	3.3	0.00205	4.2	13.52	0.44	13.18	0.55
A	**Mutt1@15**	65	7685	118	0.0359	14	9.4	12	15	0.000750	5.9	0.00228	8.3	15.15	0.90	14.69	1.22
B	**Mutt1@17**	61	5677	94	0.0212	20	15.2	5.5	5.4	0.000642	1.8	0.00197	2.2	12.98	0.23	12.69	0.28
B	**Mutt1@18**	63	5343	85	0.0292	14	10.1	11	11	0.000664	6.1	0.00202	8.8	13.43	0.82	12.98	1.14
B	**Mutt1@19**	72	8289	115	0.0258	23	10.7	11	9.3	0.000696	5.6	0.00210	6.9	14.07	0.78	13.49	0.93
B	**Mutt1@20**	78	7277	93	0.0297	15	9.33	12	12	0.000660	6.0	0.00201	8.2	13.34	0.80	12.98	1.06
C	**Mutt1@06**	133	14397	108	0.0215	12	20.0	4.6	4.1	0.000650	2.1	0.00200	2.4	13.12	0.27	12.86	0.31
C	**Mutt1@07**	179	26396	148	0.0361	9.5	25.6	5.8	5.4	0.000606	4.3	0.00187	4.7	12.24	0.52	12.06	0.56
C	**Mutt1@08**	139	8320	60	0.0235	12	11.9	3.6	7.6	0.000622	2.9	0.00188	3.9	12.57	0.36	12.13	0.47
C	**Mutt1@09**	82	3834	47	0.0253	13	8.06	7.1	12	0.000689	5.5	0.00203	8.2	13.92	0.77	13.06	1.07

	Mutt1@10	177	11891	67	0.0237	11	14.3	6.8	6.4	0.000642	2.0	0.00198	2.7	12.98	0.26	12.75	0.35
D	**Mutt1@01**	18	12754	708	0.0237	20	38.2	8.7	2.4	0.000630	1.6	0.00192	1.8	12.73	0.21	12.38	0.23
	Mutt1@02	21	13522	637	0.0451	13	33.2	11	5.2	0.000637	2.2	0.00194	2.4	12.88	0.28	12.52	0.30
	Mutt1@03	15	10784	706	0.0399	15	33.2	11	4.6	0.000628	2.6	0.00192	2.8	12.68	0.32	12.36	0.35
	Mutt1@04	20	14107	689	0.0376	15	29.2	11	5.0	0.000609	2.0	0.00185	2.2	12.31	0.24	11.94	0.26
	Mutt1@05	16	11094	675	0.0478	14	28.6	11	6.4	0.000647	2.0	0.00198	2.3	13.07	0.26	12.76	0.29
	Mutt1@16	*46*	*5987*	*131*	*0.0346*	*12*	*9.3*	*11*	*14.4*	*0.000809*	*5.7*	*0.00247*	*7.8*	*16.35*	*0.93*	*15.91*	*1.25*
A	**Unte1@13**	268	21010	78	0.0406	6.5	7.65	4.3	21	0.000789	5.1	0.00247	8.2	15.94	0.81	15.90	1.31
	Unte1@14	621	12863	21	0.0142	14	5.11	2.2	11	0.000831	2.9	0.00248	5.3	16.79	0.49	15.98	0.85
	Unte1@15	379	17116	45	0.0391	4.1	4.72	2.4	32	0.000749	3.4	0.00232	5.9	15.12	0.52	14.91	0.88
	Unte1@16	1213	40906	34	0.0476	4.8	3.11	2.0	59	0.000764	5.9	0.00222	17.3	15.45	0.91	14.30	2.47
B	**Unte1@01**	90	11906	132	0.0223	10	19.9	5.4	4.3	0.000799	1.8	0.00246	2.1	16.15	0.30	15.85	0.33
	Unte1@07	172	23543	137	0.0234	10	17.6	6.7	5.1	0.000762	2.1	0.00233	2.4	15.39	0.32	15.03	0.37
	Unte1@08	155	40208	259	0.0326	7.6	41.3	4.1	3.1	0.000772	1.8	0.00240	1.9	15.60	0.28	15.48	0.29
	Unte1@09	325	93631	288	0.0329	8.9	45.9	4.9	2.8	0.000711	1.8	0.00221	1.9	14.37	0.25	14.26	0.26
	Unte1@10	304	94723	312	0.0314	9.2	40.3	7.1	3.0	0.000733	1.9	0.00228	2.0	14.80	0.28	14.67	0.30
	Unte1@11	215	69197	321	0.0305	8.3	38.8	6.2	3.0	0.000754	1.9	0.00235	2.1	15.23	0.30	15.10	0.31
	Unte1@12	157	45164	288	0.0520	2.9	7.70	3.0	26	0.000762	2.2	0.00239	3.4	15.40	0.33	15.42	0.52
	Unte1@18	264	70111	265	0.0312	7.2	36.0	5.8	3.3	0.000761	1.9	0.00237	2.1	15.37	0.29	15.23	0.31
	Unte1@19	168	67878	404	0.0406	7.1	39.4	7.5	4.0	0.000753	2.1	0.00235	2.3	15.22	0.32	15.12	0.34
	Unte1@20	169	47601	282	0.0486	3.6	18.6	1.9	10	0.000769	2.2	0.00241	2.5	15.54	0.34	15.51	0.39
	Unte1@21	214	73456	343	0.0410	6.9	44.1	7.2	3.6	0.000703	2.0	0.00219	2.2	14.19	0.29	14.09	0.30
	Unte1@22	269	80926	300	0.0365	7.1	43.4	6.1	3.2	0.000735	1.8	0.00229	1.9	14.85	0.27	14.74	0.28
C	**Unte1@02**	158	29278	185	0.0331	7.5	17.5	8.8	7.3	0.000698	3.0	0.00215	3.7	14.11	0.42	13.87	0.51
	Unte1@03	142	29089	206	0.0322	8.0	27.5	5.1	4.5	0.000655	1.8	0.00203	2.0	13.24	0.23	13.09	0.26
	Unte1@04	234	28351	121	0.0257	11	16.2	5.8	6.1	0.000676	2.9	0.00207	3.4	13.65	0.40	13.34	0.46

	Unte1@05	359	67280	187	0.0300	10	21.3	8.2	5.4	0.000620	2.3	0.00191	2.8	12.53	0.29	12.32	0.35
	Unte1@06	*469*	*8977*	*19*	*0.0167*	*13*	*4.0*	*4.8*	*16*	*0.000891*	*7.2*	*0.00254*	*15.6*	*18.00*	*1.29*	*16.33*	*2.54*
A	**Cavr1@01**	68	11689	172	0.0201	15	39.5	3.1	2.0	0.00100	3.2	0.00314	3.4	20.18	0.64	20.18	0.68
	Cavr1@02	61	10663	175	0.0203	18	38.2	2.2	2.1	0.000914	1.6	0.00287	1.8	18.46	0.30	18.46	0.32
	Cavr1@03	116	25657	222	0.0301	13	36.0	6.7	3.2	0.000767	2.8	0.00239	2.9	15.51	0.43	15.39	0.45
	Cavr1@04	65	9997	154	0.0219	28	33.3	3.6	2.5	0.00100	1.8	0.00314	1.9	20.18	0.36	20.18	0.39
	Cavr1@05	89	15180	171	0.0289	11	42.4	1.4	2.6	0.000844	1.5	0.00265	1.6	17.05	0.26	17.06	0.27
	Cavr1@06	92	20316	222	0.0356	11	44.1	3.6	3.1	0.000892	1.5	0.00279	1.6	18.03	0.27	17.95	0.29
B	**Cavr1@07**	65	12213	188	0.0311	12	29.3	6.5	4.1	0.000888	3.1	0.00276	3.4	17.94	0.56	17.77	0.60
	Cavr1@08	117	24045	205	0.0293	14	21.9	10	5.2	0.000618	2.5	0.00191	3.0	12.48	0.31	12.27	0.37
	Cavr1@09	131	23106	176	0.0275	15	22.4	8.5	4.7	0.000689	2.6	0.00214	2.9	13.92	0.36	13.76	0.40
	Cavr1@10	130	21198	164	0.0175	21	28.4	4.1	2.4	0.000732	1.1	0.00228	1.2	14.80	0.16	14.68	0.17
	Cavr1@11	202	44351	220	0.0344	16	28.1	6.2	4.7	0.000612	2.3	0.00188	2.5	12.36	0.28	12.13	0.31
	Cavr1@12	107	16435	153	0.0205	19	30.4	2.1	2.6	0.000578	2.0	0.00180	2.2	11.68	0.24	11.57	0.26
C	**Cavr1@13**	86	17142	200	0.0413	11	18.7	7.2	8.5	0.000710	2.7	0.00220	3.4	14.34	0.38	14.15	0.49
	Cavr1@14	104	20617	199	0.0372	14	19.8	5.4	7.3	0.000657	2.4	0.00204	2.9	13.28	0.32	13.13	0.38
	Cavr1@15	85	18722	221	0.0345	15	18.2	7.1	7.3	0.000668	3.0	0.00205	3.5	13.50	0.40	13.23	0.46
	Cavr1@16	53	11560	217	0.0336	10	18.4	6.8	7.0	0.000721	2.4	0.00224	2.9	14.56	0.35	14.41	0.42
	Cavr1@17	50	8775	176	0.0417	10	16.2	7.0	9.9	0.000695	3.0	0.00214	3.6	14.03	0.42	13.80	0.50
	Cavr1@18	206	21752	105	0.0228	11	17.7	5.8	5.0	0.000761	2.7	0.00234	3.2	15.37	0.42	15.04	0.48
	Cavr1@19	241	27925	116	0.0195	12	21.7	4.0	3.5	0.000685	2.5	0.00212	2.8	13.85	0.34	13.64	0.38
	Cavr1@20	292	36265	124	0.0177	14	21.9	4.1	3.1	0.000675	2.1	0.00208	2.3	13.64	0.28	13.39	0.31
	Cavr1@21	367	44092	120	0.0188	13	20.5	4.3	3.5	0.000655	2.3	0.00201	2.6	13.24	0.30	12.95	0.34
	Cavr1@22	214	26215	123	0.0236	12	20.9	4.4	4.4	0.000687	2.4	0.00211	2.7	13.89	0.34	13.60	0.37
D	**Cavr1@23**	266	204961	771	0.0798	5.1	92.6	5.3	3.3	0.000693	2.0	0.00216	2.0	13.99	0.27	13.93	0.28
	Cavr1@24	207	144862	699	0.0776	9.0	83.3	4.4	3.6	0.000672	2.0	0.00210	2.1	13.58	0.28	13.51	0.28

	Cavr1@25	172	42448	247	0.0326	8.1	35.4	5.8	3.6	0.000700	2.0	0.00218	2.2	14.15	0.28	14.04	0.31
	Cavr1@26	*283*	*167109*	*591*	*0.0414*	*8.5*	*61.9*	*6.0*	*2.6*	*0.000572*	*2.2*	*0.00178*	*2.3*	*11.56*	*0.25*	*11.48*	*0.26*
	Cavr1@27	*617*	*212408*	*344*	*0.0308*	*11*	*46.6*	*5.7*	*2.6*	*0.000523*	*3.0*	*0.00162*	*3.2*	*10.56*	*0.32*	*10.45*	*0.33*
A	**Gott1@01**	297	14289	48	0.0166	8.6	8.85	2.8	7.2	0.000678	2.3	0.00201	3.4	13.71	0.32	12.97	0.43
	Gott1@02	323	14908	46	0.0171	9.0	8.96	2.3	7.4	0.000657	2.5	0.00196	3.5	13.27	0.33	12.63	0.44
	Gott1@03	238	11380	48	0.0161	15	8.73	2.7	7.1	0.000689	2.4	0.00204	3.5	13.93	0.33	13.13	0.46
	Gott1@04	260	13187	51	0.0173	8.8	8.54	3.0	7.8	0.000663	2.6	0.00195	3.6	13.39	0.35	12.54	0.45
	Gott1@05	256	13817	54	0.0227	7.05	8.26	4.9	11	0.000748	2.6	0.00219	4.1	15.11	0.39	14.09	0.58
	Gott1@06	393	25054	64	0.0247	8.5	9.15	3.9	10	0.000724	2.5	0.00218	3.4	14.62	0.36	14.05	0.47
	Gott1@07	342	18284	53	0.0222	6.8	9.12	2.2	9.4	0.000692	2.8	0.00211	3.8	13.99	0.39	13.58	0.52
	Gott1@08	463	31403	68	0.0231	10	8.46	5.3	11	0.000733	3.5	0.00220	4.9	14.82	0.51	14.18	0.70
	Gott1@09	757	51462	68	0.0243	12	8.21	6.8	11	0.000722	4.2	0.00217	6.3	14.60	0.62	13.96	0.88
	Gott1@10	602	37021	61	0.0260	14	9.03	4.5	11	0.000689	2.9	0.00208	4.0	13.93	0.40	13.42	0.54
B	**Gott1@12**	766	6895	9	0.00836	10	2.54	1.8	13	0.000700	3.9	0.00153	25.4	14.15	0.55	9.87	2.51
	Gott1@13	1712	37257	22	0.00951	7.9	5.76	0.6	6.4	0.000648	1.9	0.00193	3.1	13.09	0.24	12.41	0.38
	Gott1@14	2404	57977	24	0.00901	10	5.95	1.2	5.9	0.000600	1.9	0.00176	3.4	12.13	0.23	11.31	0.38
	Gott1@15	2403	58426	24	0.00830	11	5.84	0.9	5.5	0.000608	2.3	0.00177	3.9	12.28	0.28	11.39	0.44
	Gott1@16	635	13426	21	0.0115	9.3	5.44	1.9	8.1	0.000746	2.4	0.00222	4.4	15.08	0.35	14.29	0.63
	Gott1@17	548	10933	20	0.00790	12	5.12	1.8	6.0	0.000672	2.7	0.00196	5.1	13.57	0.36	12.65	0.64
	Gott1@18	893	17119	19	0.00827	11	5.11	1.6	6.2	0.000680	2.7	0.00202	5.1	13.74	0.37	13.00	0.66
	Gott1@19	772	13152	17	0.00960	10	4.30	1.9	8.6	0.000672	2.2	0.00186	5.3	13.57	0.30	12.00	0.64
	Gott1@20	937	15181	16	0.00784	11	4.31	0.9	7.0	0.000647	2.4	0.00185	5.0	13.07	0.31	11.94	0.59
	Gott1@11	*1193*	*18132*	*15*	*0.0110*	*24*	*3.9*	*2.4*	*10.9*	*0.000824*	*4.2*	*0.00233*	*9.7*	*16.64*	*0.70*	*15.01*	*1.45*

Table 4. Th-U-Pb analyses of monazite by ion microprobe (Nordsim)

Aar Massif Groups	Analysis ID	U (ppm)	Th (ppm)	Th/U	$^{208}Pb/^{204}Pb$	1σ (%)	f208 (%)	204 and $ThNdO_2$ - corr $^{208}Pb/^{232}Th$	1σ (%)	204 and $ThNdO_2$ - corr spot ages $^{232}Th/^{208}Pb$ Age (Ma)	1σ (abs.)
A	**Gutt1@01**	107	9091	85	290	22	0.0	0.000430	7.2	8.68	0.62
	Gutt1@03	338	13143	39	1490	28	2.6	0.000705	6.6	14.24	0.94
B	**Gutt1@02**	167	9837	59	818	14	0.0	0.000481	4.7	9.72	0.45
	Gutt1@06	122	9038	74	3470	67	0.0	0.000686	9.3	13.86	1.29
	Gutt1@07	41	2662	66	2740	37	1.1	0.000480	4.8	9.69	0.47
	Gutt1@08	*83*	*8602*	*2*	*5940*	*70*	*0.0*	*0.000686*	*23.8*	*13.86*	*3.30*
	Gutt1@09	*109*	*10834*	*2*	*1035*	*44*	*0.7*	*0.000790*	*16.2*	*15.96*	*2.59*
A	**Gosch1@08**	75	14351	192	589	8.4	4.9	0.000606	3.3	12.25	0.40
	Gosch1@09	61	11270	186	666	10	3.3	0.000623	3.3	12.59	0.42
B	**Gosch1@11**	204	8973	44	240	8.9	15	0.000607	3.3	12.26	0.40
	Gosch1@12	118	4257	36	250	10	15	0.000639	3.5	12.92	0.45
	Gosch1@13	132	4184	32	239	10	12	0.000611	3.6	12.35	0.44
	Gosch1@14	126	8045	64	309	7.8	10	0.000606	3.4	12.25	0.41
	Gosch1@15	159	5366	34	371	11	7.8	0.000556	3.5	11.24	0.40
	Gosch1@16	189	7445	39	414	11	7.8	0.000598	3.4	12.08	0.41
	Gosch1@17	170	9138	54	332	8.2	8.7	0.000558	3.3	11.27	0.37
C	**Gosch1@01**	108	5598	52	508	12	6.0	0.000602	3.4	12.17	0.42
	Gosch1@02	214	3901	18	329	13	10	0.000597	3.9	12.07	0.47
	Gosch1@03	279	5321	19	603	18	5.0	0.000565	4.0	11.41	0.46
	Gosch1@04	287	5458	19	440	15	8.3	0.000550	3.6	11.11	0.40

	Gosch1@05	386	6508	17	706	20	3.4	0.000478	3.9	9.66	0.37
	Gosch1@06	426	8778	21	798	19	4.4	0.000442	3.9	8.94	0.35
	Gosch1@07	*2095*	*9676*	*5*	*695*	*14*	*2.9*	*0.000665*	*3.5*	*13.44*	*0.46*
	Gosch1@10	*38*	*12802*	*340*	*702*	*13*	*4.9*	*0.000517*	*3.4*	*10.45*	*0.35*
A	**Salz21@06**	69	10890	158	393	7.4	6.8	0.000527	3.0	10.64	0.32
	Salz21@08	88	10157	115	581	10	5.4	0.000541	3.1	10.93	0.34
	Salz21@09	72	7387	103	352	8.1	8.4	0.000522	3.0	10.55	0.32
	Salz21@12	76	15536	205	532	8.0	4.0	0.000563	3.0	11.38	0.34
	Salz21@13	87	17475	200	653	11	4.1	0.000548	3.0	11.08	0.34
B	**Salz21@01**	169	12991	77	484	8.6	5.6	0.000519	3.0	10.50	0.32
	Salz21@02	197	14058	72	791	9.2	2.2	0.000535	3.1	10.80	0.33
	Salz21@03	224	15079	67	1091	11	1.5	0.000547	3.1	11.05	0.34
	Salz21@04	226	16234	72	651	9.3	3.2	0.000514	3.1	10.38	0.32
	Salz21@05	222	15960	72	691	13	3.0	0.000518	3.1	10.47	0.33
	Salz21@07	*90*	*10004*	*111*	*464*	*11*	*5.9*	*0.000485*	*3.1*	*9.80*	*0.30*
	Salz21@10	*91*	*7304*	*80*	*345*	*13*	*9.1*	*0.000473*	*3.4*	*9.56*	*0.33*
	Salz21@11	*128*	*9589*	*75*	*235*	*12*	*16*	*0.000414*	*3.5*	*8.36*	*0.29*

Table A.1. Supplementary Th-U-Pb analyses (Nordsim) of monazite from Griesserental fissure (Janots et al., 2012)

Griesserental (Aar Massif)							**204 and $ThNdO_2$ - corr**		**204 and $ThNdO_2$ - corr spot ages**	
Analysis ID	**U (ppm)**	**Th (ppm)**	**Th/U**	**$^{208}Pb/^{204}Pb$**	**1σ (%)**	**f208 (%)**	**$^{208}Pb/^{232}Th$**	**1σ (%)**	**$^{232}Th/^{208}Pb$ Age (Ma)**	**1σ (abs.)**
Griess3_1@1	65	27035	414	1995	14	1.9	0.000629	1.2	12.71	0.15
Griess3_1@2	66	26017	395	3915	30	1.0	0.000635	1.2	12.83	0.15
Griess3_1@3	66	25449	385	2941	24	1.3	0.000632	1.2	12.78	0.15
Griess3_1@4	71	27520	386	4169	32	0.9	0.000635	1.2	12.83	0.15
Griess3_1@5	74	25752	347	1947	15	2.0	0.000631	1.2	12.74	0.15
Griess3_1@6	120	25966	216	1556	14	2.5	0.000631	1.4	12.76	0.18
Griess3_1@7	370	31370	85	1952	17	2.0	0.000623	1.5	12.60	0.19
Griess3_1@9	385	28972	75	1429	11	2.7	0.000617	1.2	12.48	0.15
Griess3_1@10	254	35531	140	2012	13	1.9	0.000638	1.1	12.90	0.14
Griess3_1@11	306	27066	88	1300	10	3.0	0.000630	1.1	12.73	0.14
Griess3_1@12	289	38183	132	1858	12	2.1	0.000643	1.1	13.00	0.15
Griess3_2@1	121	27472	228	2944	25	1.3	0.000636	1.2	12.86	0.15
Griess3_2@2	120	25172	211	1541	13	2.5	0.000636	1.2	12.85	0.15
Griess3_2@4	237	60969	257	1557	7.5	2.5	0.000617	1.1	12.46	0.14
Griess3_2@5	162	42999	266	3127	20	1.2	0.000627	1.1	12.67	0.14
Griess3_2@6	152	41769	276	2678	16	1.4	0.000616	1.2	12.45	0.15
Griess3_2@7	167	49029	293	2389	13	1.6	0.000616	1.2	12.45	0.15
Griess3_2@8	85	45513	536	2019	12	1.9	0.000614	1.2	12.41	0.15

Table A.2. Supplementary electron microprobe analyses of monazite grains GOSCH1 and SALZ21

	Gosch 1@1	Gosch 1@2	Gosch 1@3	Gosch 1@4	Gosch 1@5	Gosch 1@6	Gosch 1@7	Gosch 1@8	Salz21 @1	Salz21 @2	Salz21 @3	Salz21 @4	Salz21 @5	Salz21 @6	Salz21 @7	Salz21 @8
P2O5	28.09	28.07	28.03	28.15	28.82	28.82	28.75	28.80	28.32	28.26	28.26	28.51	28.77	28.75	28.63	28.64
ThO2	0.32	0.56	0.15	0.53	0.42	0.31	0.31	0.27	1.32	1.37	1.32	1.30	0.43	0.55	0.50	0.58
UO2	b.d.	b.d.	b.d.	b.d.	b.d.	b.d.	b.d.	b.d.	b.d.	b.d.	b.d.	b.d.	b.d.	b.d.	b.d.	b.d.
SiO2	0.10	0.10	0.10	0.11	0.11	0.10	0.10	0.10	0.21	0.22	0.21	0.23	0.12	0.10	0.14	0.14
Al2O3	b.d.	b.d.	b.d.	b.d.	b.d.	b.d.	b.d.	b.d.	b.d.	b.d.	b.d.	b.d.	b.d.	b.d.	b.d.	b.d.
Y2O3	1.08	1.03	1.00	1.04	0.90	0.94	0.91	0.91	0.51	0.57	0.52	0.55	0.50	0.50	0.68	0.69
La2O3	15.59	15.93	15.27	15.75	14.66	14.61	14.75	14.67	15.44	15.21	15.15	15.21	16.98	17.28	15.38	15.50
Ce2O3	32.18	33.76	33.21	32.97	33.54	33.52	33.19	33.23	32.45	32.47	32.22	32.53	33.19	32.71	32.14	32.37
Pr2O3	3.19	2.95	3.08	3.35	3.42	3.38	3.38	3.39	2.98	3.42	3.19	3.18	3.17	3.04	3.36	3.33
Nd2O3	11.80	12.12	12.26	11.63	12.75	12.51	12.28	12.25	12.07	12.57	12.71	12.56	11.27	11.27	12.43	12.69
Sm2O3	2.50	2.39	2.56	2.44	2.44	2.64	2.40	2.42	2.19	2.23	2.15	2.24	1.93	1.96	2.24	2.22
Eu2O3	b.d.	b.d.	b.d.	b.d.	b.d.	b.d.	b.d.	b.d.	b.d.	b.d.	b.d.	b.d.	b.d.	b.d.	b.d.	b.d.
Gd2O3	1.55	1.42	1.54	1.51	1.56	1.60	1.57	1.63	1.36	1.36	1.36	1.37	1.10	1.05	1.50	1.39
Tb2O3	b.d.	b.d.	b.d.	b.d.	b.d.	b.d.	b.d.	b.d.	b.d.	b.d.	b.d.	b.d.	b.d.	b.d.	b.d.	b.d.
Dy2O3	0.23	0.28	0.17	0.19	0.24	0.28	0.16	0.24	0.19	0.17	0.15	0.18	0.08	0.14	0.14	0.22
CaO	0.24	0.25	0.22	0.24	0.10	0.09	0.09	0.09	0.14	0.14	0.14	0.14	0.18	0.18	0.09	0.10
SrO	b.d.	b.d.	b.d.	b.d.	b.d.	b.d.	b.d.	b.d.	b.d.	b.d.	b.d.	b.d.	0.07	0.07	b.d.	b.d.
PbO	b.d.	b.d.	b.d.	b.d.	b.d.	b.d.	b.d.	b.d.	0.11	0.08	b.d.	0.07	b.d.	b.d.	b.d.	b.d.
Total	96.93	98.93	97.64	97.93	98.99	98.80	97.89	98.02	97.35	98.12	97.48	98.14	97.83	97.59	97.26	97.89
Normalized to P+Si = 1pfu																
P	0.996	0.996	0.996	0.996	0.996	0.996	0.996	0.996	0.991	0.991	0.991	0.991	0.995	0.996	0.994	0.994
Th	0.003	0.005	0.001	0.005	0.004	0.003	0.003	0.003	0.012	0.013	0.012	0.012	0.004	0.005	0.005	0.005
U	0.000	0.000	0.000	0.000	0.000	0.000	0.000	0.000	0.000	0.000	0.000	0.000	0.000	0.000	0.000	0.000
Si	0.004	0.004	0.004	0.004	0.004	0.004	0.004	0.004	0.009	0.009	0.009	0.009	0.005	0.004	0.006	0.006
Al	0.000	0.000	0.000	0.000	0.000	0.000	0.000	0.000	0.000	0.000	0.000	0.000	0.000	0.000	0.000	0.000
Y	0.024	0.023	0.022	0.023	0.020	0.020	0.020	0.020	0.011	0.013	0.012	0.012	0.011	0.011	0.015	0.015
La	0.241	0.246	0.236	0.243	0.221	0.220	0.223	0.221	0.235	0.232	0.232	0.230	0.256	0.261	0.233	0.234
Ce	0.493	0.518	0.510	0.504	0.501	0.501	0.497	0.497	0.491	0.492	0.489	0.489	0.497	0.490	0.483	0.486
Pr	0.049	0.045	0.047	0.051	0.051	0.050	0.050	0.050	0.045	0.052	0.048	0.048	0.047	0.045	0.050	0.050

Nd	0.176	0.181	0.184	0.174	0.186	0.182	0.179	0.179	0.178	0.186	0.188	0.184	0.164	0.165	0.182	0.186
Sm	0.036	0.035	0.037	0.035	0.034	0.037	0.034	0.034	0.031	0.032	0.031	0.032	0.027	0.028	0.032	0.031
Gd	0.022	0.020	0.021	0.021	0.021	0.022	0.021	0.022	0.019	0.019	0.019	0.019	0.015	0.014	0.020	0.019
Tb	0.000	0.000	0.000	0.000	0.000	0.000	0.000	0.000	0.000	0.000	0.000	0.000	0.000	0.000	0.000	0.000
Dy	0.003	0.004	0.002	0.003	0.003	0.004	0.002	0.003	0.003	0.002	0.002	0.002	0.001	0.002	0.002	0.003
Ca	0.011	0.011	0.010	0.011	0.004	0.004	0.004	0.004	0.006	0.006	0.006	0.006	0.008	0.008	0.004	0.004
Sr	0.000	0.000	0.000	0.000	0.000	0.000	0.000	0.000	0.000	0.000	0.000	0.000	0.002	0.002	0.000	0.000
Pb	0.000	0.000	0.000	0.000	0.000	0.000	0.000	0.000	0.001	0.001	0.000	0.001	0.000	0.000	0.000	0.000
Sum Cations	2.058	2.088	2.072	2.069	2.045	2.043	2.033	2.032	2.033	2.047	2.038	2.035	2.032	2.030	2.025	2.034

- In-situ Th-Pb dating of fissure monazite is a reliable method for studying shear zone activity between ~350 – 200 ℃
- Relation of fissure monazite domain ages with field structures
- Fissure monazite grows over several millions of years

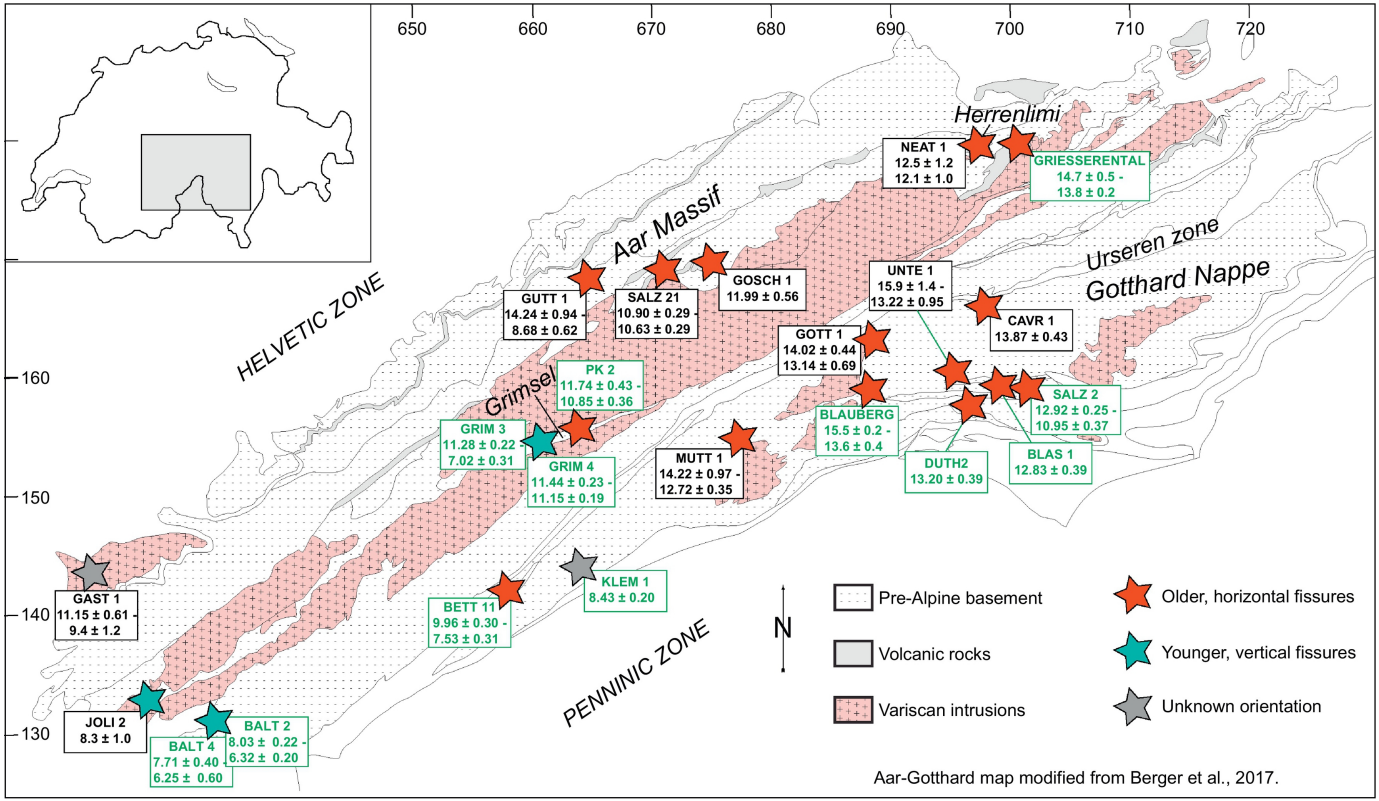
650
660
670
680
690
700
710
720
160
150
140
130
HELVETIC ZONE
Aar Massif
Grimsel
Herrenlimi
Urseren zone
Gotthard Nappe
PENNINIC ZONE
N
NEAT 1
12.5 ± 1.2
12.1 ± 1.0
GRIESSERENTAL
14.7 ± 0.5 -
13.8 ± 0.2
GUTT 1
14.24 ± 0.94 -
8.68 ± 0.62
SALZ 21
10.90 ± 0.29 -
10.63 ± 0.29
GOSCH 1
11.99 ± 0.56
UNTE 1
15.9 ± 1.4 -
13.22 ± 0.95
CAVR 1
13.87 ± 0.43
GOTT 1
14.02 ± 0.44
13.14 ± 0.69
PK 2
11.74 ± 0.43 -
10.85 ± 0.36
GRIM 3
11.28 ± 0.22 -
7.02 ± 0.31
GRIM 4
11.44 ± 0.23 -
11.15 ± 0.19
MUTT 1
14.22 ± 0.97 -
12.72 ± 0.35
BLAUBERG
15.5 ± 0.2 -
13.6 ± 0.4
SALZ 2
12.92 ± 0.25 -
10.95 ± 0.37
DUTH2
13.20 ± 0.39
BLAS 1
12.83 ± 0.39
GAST 1
11.15 ± 0.61 -
9.4 ± 1.2
BETT 11
9.96 ± 0.30 -
7.53 ± 0.31
KLEM 1
8.43 ± 0.20
JOLI 2
8.3 ± 1.0
BALT 4
7.71 ± 0.40 -
6.25 ± 0.60
BALT 2
8.03 ± 0.22 -
6.32 ± 0.20
Pre-Alpine basement
Volcanic rocks
Variscan intrusions
Older, horizontal fissures
Younger, vertical fissures
Unknown orientation
Aar-Gotthard map modified from Berger et al., 2017.

Figure 1

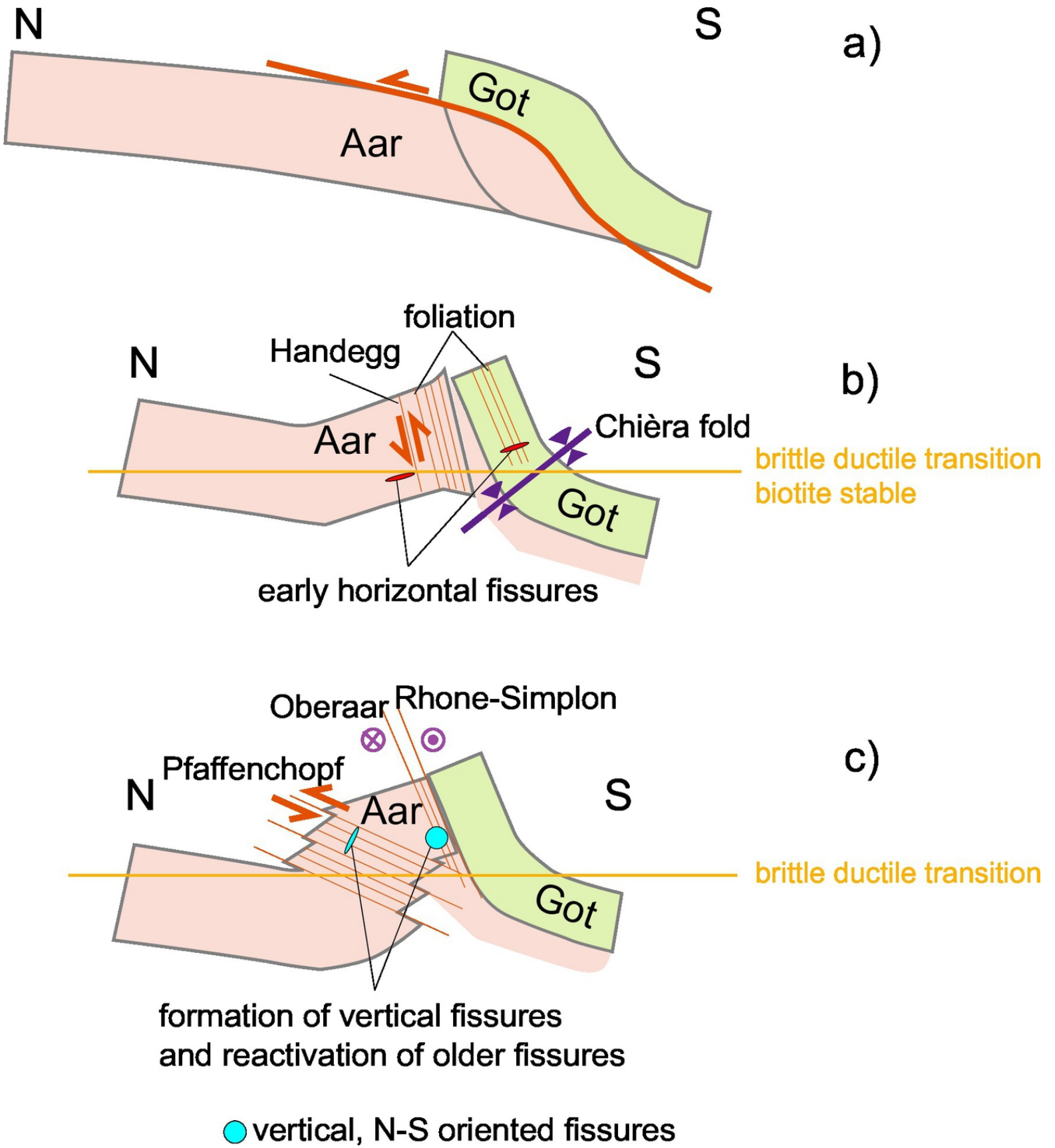
N
S
a)
Got
Aar
foliation
Handegg
N
S
b)
Aar
Chièra fold
brittle ductile transition
biotite stable
Got
early horizontal fissures
Oberaar
Rhone-Simplon
Pfaffenchopf
N
S
c)
Aar
brittle ductile transition
Got
formation of vertical fissures
and reactivation of older fissures
vertical, N-S oriented fissures

Figure 2

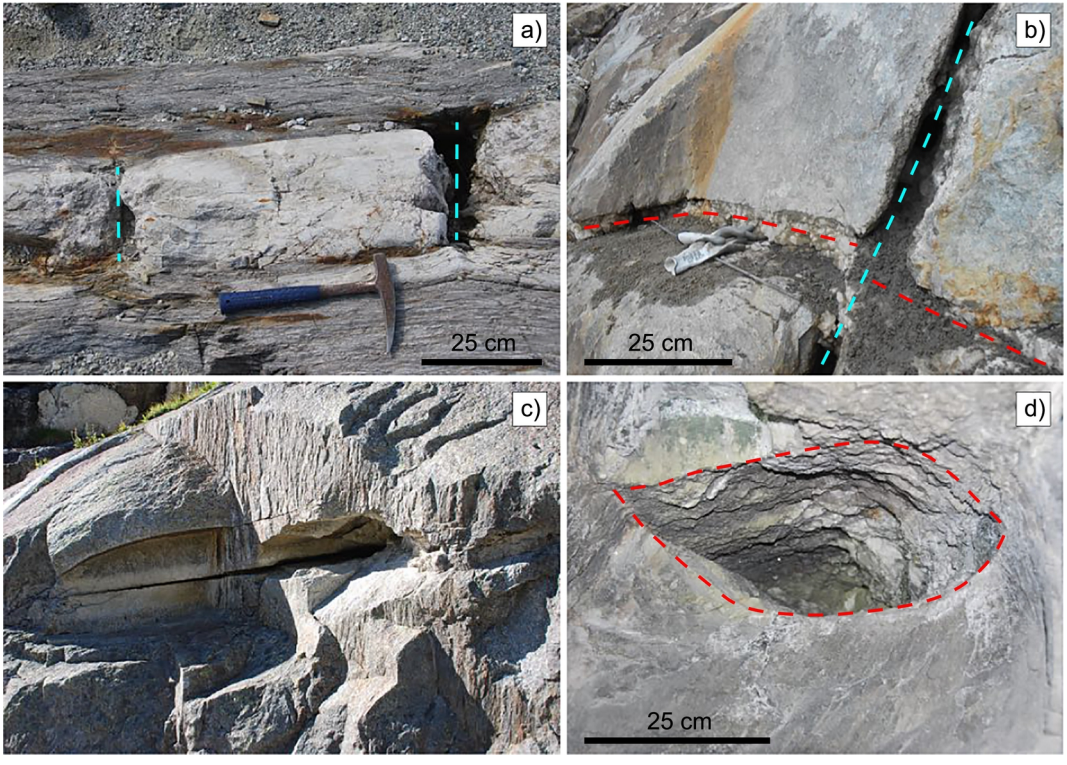

Figure 3

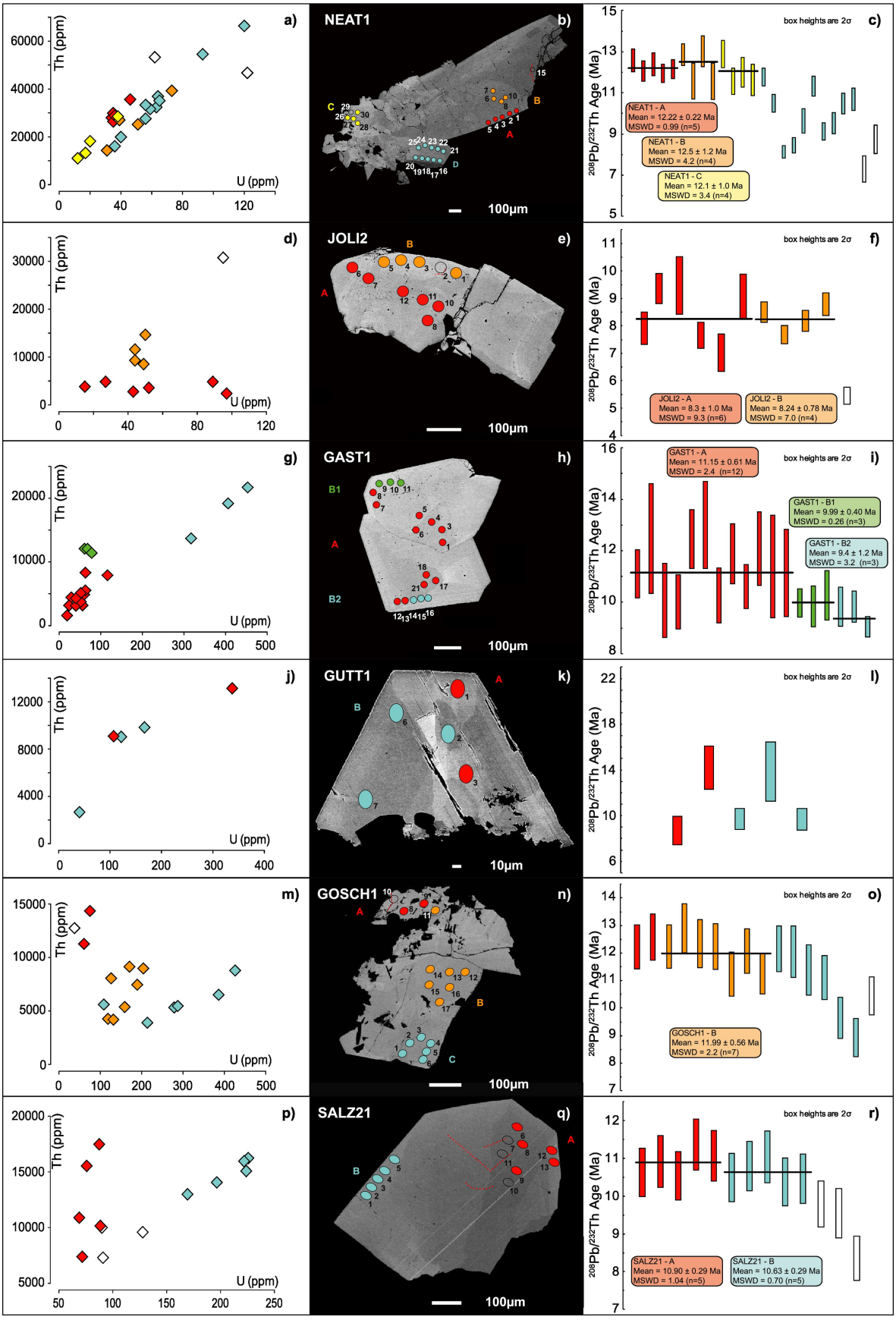
a)
Th (ppm)
U (ppm)
NEAT1
b)
100µm
c)
box heights are 2σ
NEAT1 - A
Mean = 12.22 ± 0.22 Ma
MSWD = 0.99 (n=5)
NEAT1 - B
Mean = 12.5 ± 1.2 Ma
MSWD = 4.2 (n=4)
NEAT1 - C
Mean = 12.1 ± 1.0 Ma
MSWD = 3.4 (n=4)
208Pb/232Th Age (Ma)
d)
JOLI2
e)
f)
JOLI2 - A
Mean = 8.3 ± 1.0 Ma
MSWD = 9.3 (n=6)
JOLI2 - B
Mean = 8.24 ± 0.78 Ma
MSWD = 7.0 (n=4)
g)
GAST1
h)
i)
GAST1 - A
Mean = 11.15 ± 0.61 Ma
MSWD = 2.4 (n=12)
GAST1 - B1
Mean = 9.99 ± 0.40 Ma
MSWD = 0.26 (n=3)
GAST1 - B2
Mean = 9.4 ± 1.2 Ma
MSWD = 3.2 (n=3)
j)
GUTT1
k)
10µm
l)
m)
GOSCH1
n)
o)
GOSCH1 - B
Mean = 11.99 ± 0.56 Ma
MSWD = 2.2 (n=7)
p)
SALZ21
q)
r)
SALZ21 - A
Mean = 10.90 ± 0.29 Ma
MSWD = 1.04 (n=5)
SALZ21 - B
Mean = 10.63 ± 0.29 Ma
MSWD = 0.70 (n=5)

Figure 4

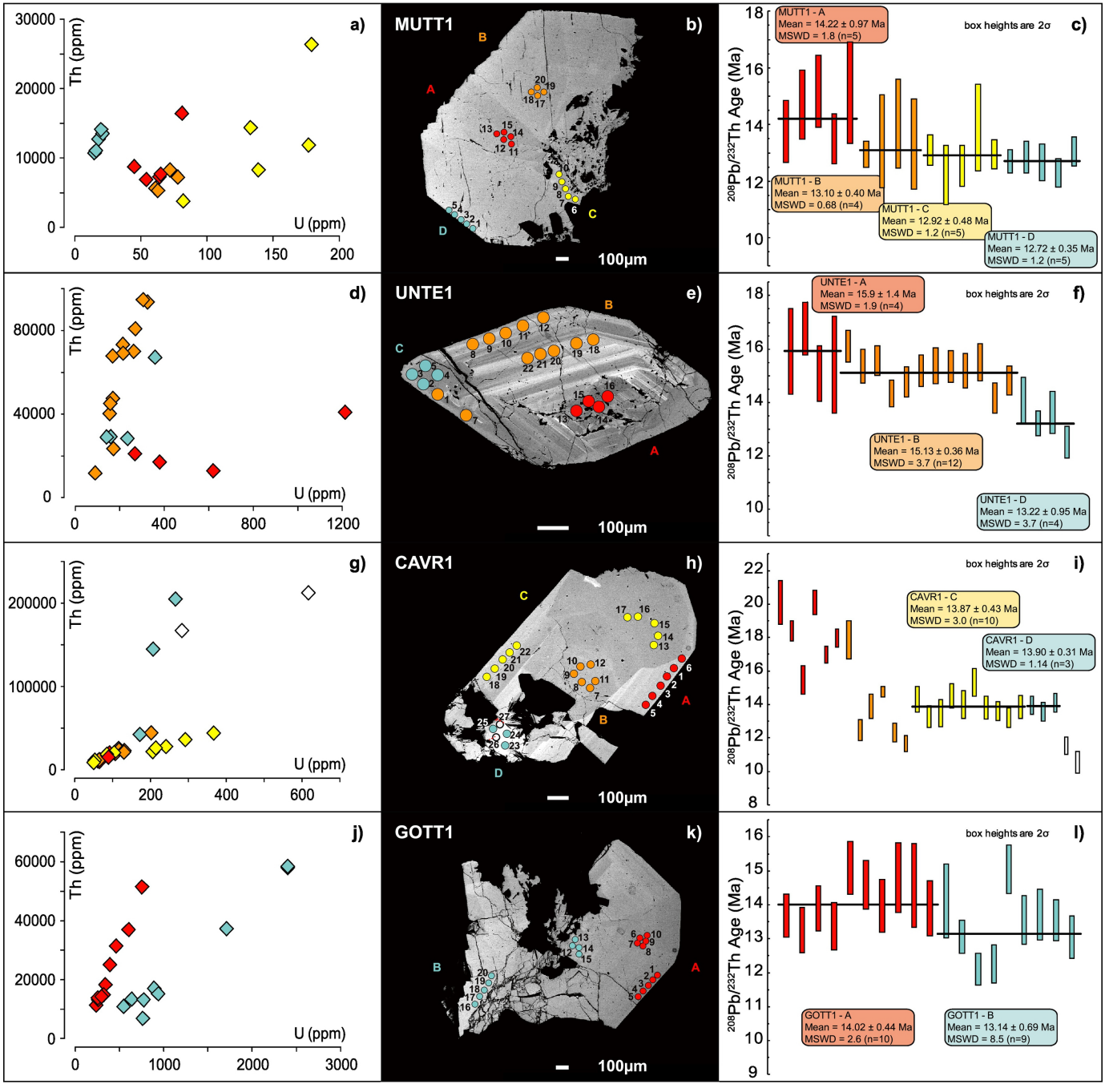
a)
Th (ppm)
U (ppm)
MUTT1
b)
100µm
c)
box heights are 2σ
MUTT1 - A
Mean = 14.22 ± 0.97 Ma
MSWD = 1.8 (n=5)
MUTT1 - B
Mean = 13.10 ± 0.40 Ma
MSWD = 0.68 (n=4)
MUTT1 - C
Mean = 12.92 ± 0.48 Ma
MSWD = 1.2 (n=5)
MUTT1 - D
Mean = 12.72 ± 0.35 Ma
MSWD = 1.2 (n=5)
208Pb/232Th Age (Ma)
d)
UNTE1
e)
f)
UNTE1 - A
Mean = 15.9 ± 1.4 Ma
MSWD = 1.9 (n=4)
UNTE1 - B
Mean = 15.13 ± 0.36 Ma
MSWD = 3.7 (n=12)
UNTE1 - D
Mean = 13.22 ± 0.95 Ma
MSWD = 3.7 (n=4)
g)
CAVR1
h)
i)
CAVR1 - C
Mean = 13.87 ± 0.43 Ma
MSWD = 3.0 (n=10)
CAVR1 - D
Mean = 13.90 ± 0.31 Ma
MSWD = 1.14 (n=3)
j)
GOTT1
k)
l)
GOTT1 - A
Mean = 14.02 ± 0.44 Ma
MSWD = 2.6 (n=10)
GOTT1 - B
Mean = 13.14 ± 0.69 Ma
MSWD = 8.5 (n=9)

Figure 5

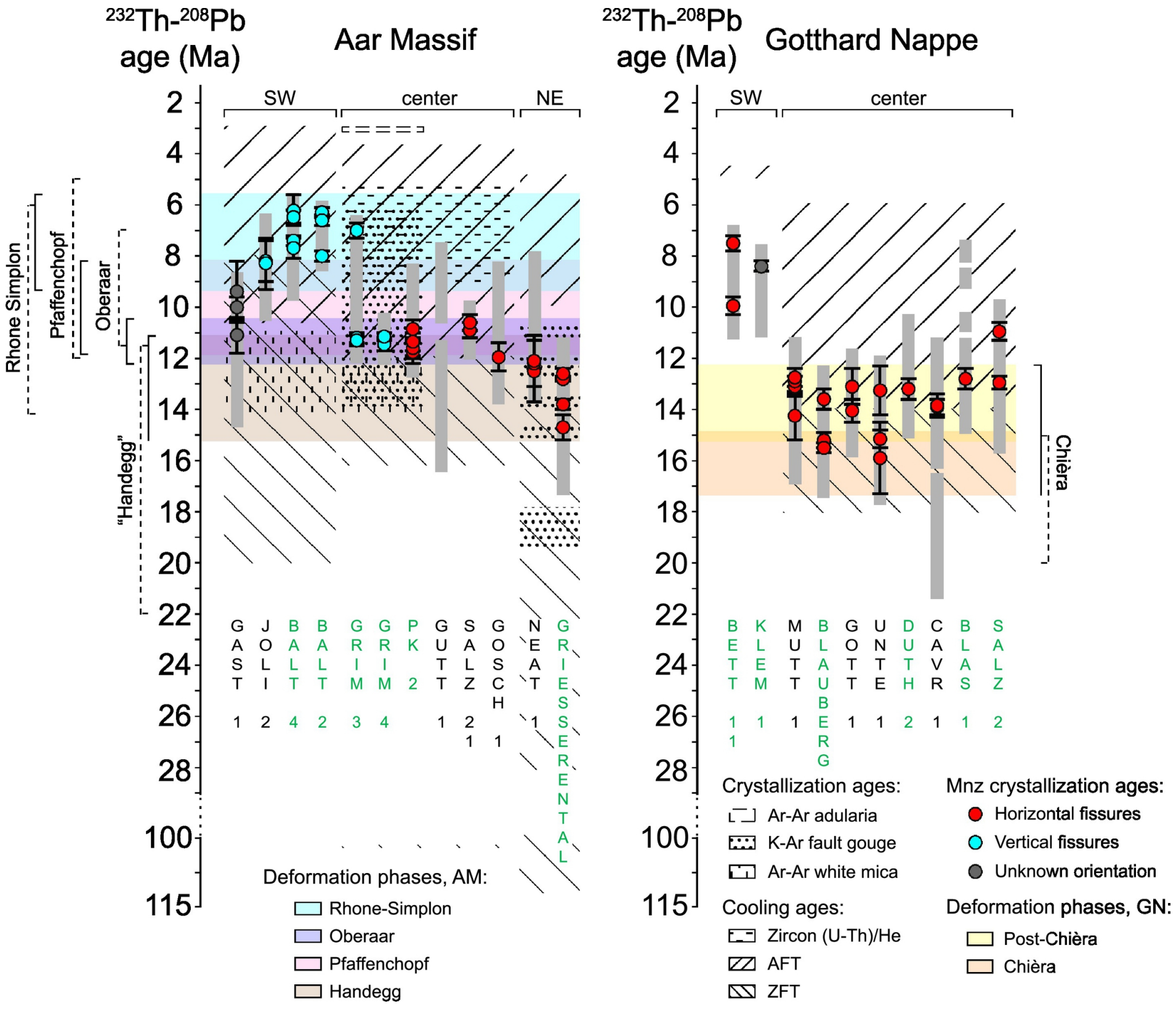
232Th-208Pb age (Ma)
Aar Massif
232Th-208Pb age (Ma)
Gotthard Nappe
SW
center
NE
SW
center
2
4
6
8
10
12
14
16
18
20
22
24
26
28
100
115
Rhone Simplon
Pfaffenchopf
Oberaar
"Handegg"
Chièra
GAST 1
JOLI 2
BALT 4
BALT 2
GRIM 3
GRIM 4
PK 2
GUTT 1
SALZ 21
GOSCH 1
NEAT 1
GRIESSERENTAL
BETT 11
KLEM 1
MUTT 1
BLAUBERG
GOTT 1
UNTE 1
DUTH 2
CAVR 1
BLAS 1
SALZ 2
Deformation phases, AM:
Rhone-Simplon
Oberaar
Pfaffenchopf
Handegg
Crystallization ages:
Ar-Ar adularia
K-Ar fault gouge
Ar-Ar white mica
Cooling ages:
Zircon (U-Th)/He
AFT
ZFT
Mnz crystallization ages:
Horizontal fissures
Vertical fissures
Unknown orientation
Deformation phases, GN:
Post-Chièra
Chièra

Figure 6

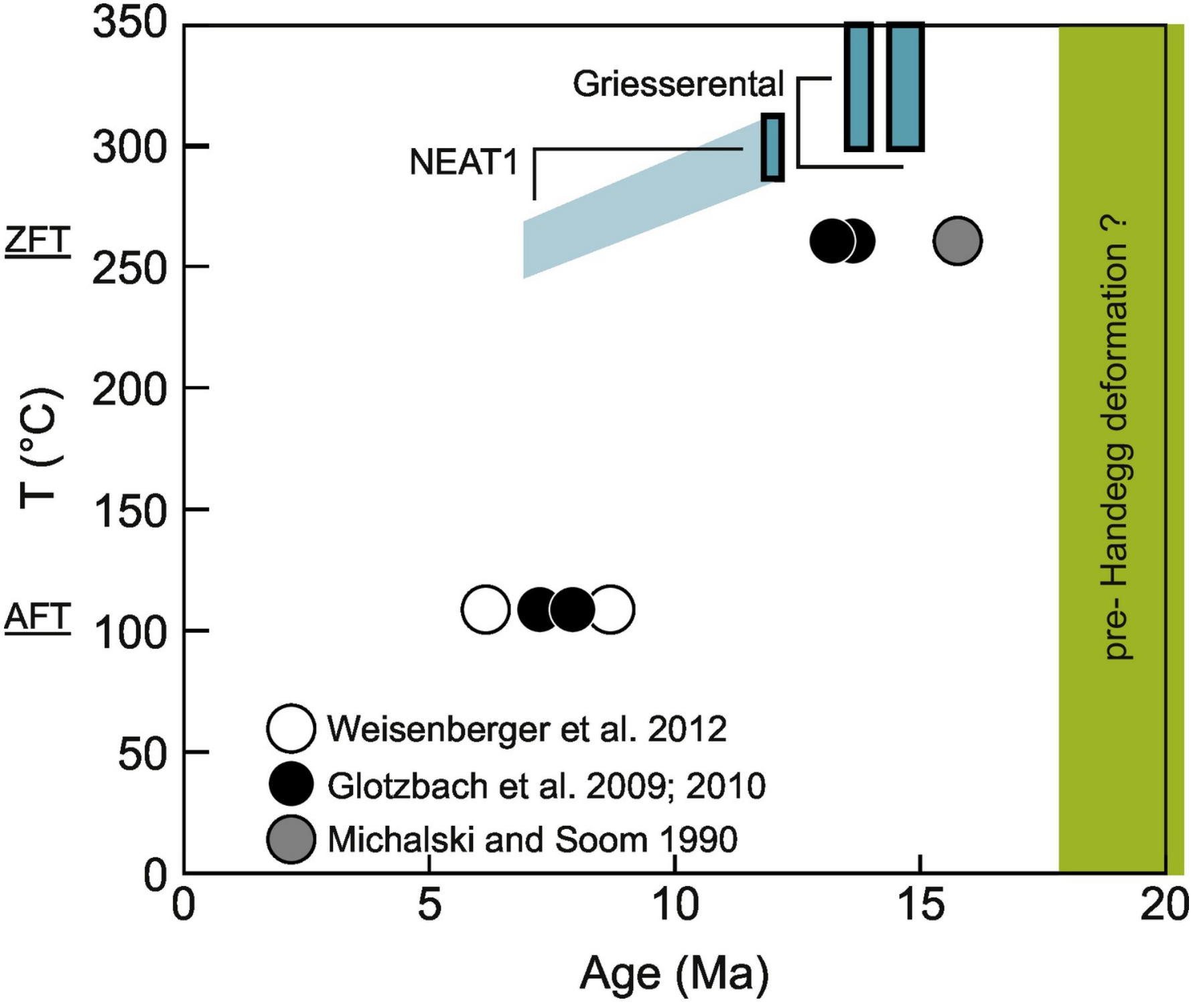
350
300
250
200
150
100
50
0
ZFT
AFT
T (°C)
Griesserental
NEAT1
pre- Handegg deformation ?
Weisenberger et al. 2012
Glotzbach et al. 2009; 2010
Michalski and Soom 1990
0
5
10
15
20
Age (Ma)

Figure 7